Global and Planetary Change 142 (2016) 53–72

Contents lists available at ScienceDirect

Global and Planetary Change

journal homepage: www.elsevier.com/locate/gloplacha

Marine response to climate changes during the last five millennia in the central Mediterranean Sea

G. Margaritelli [a,b,*], M. Vallefuoco [a], F. Di Rita [c], L. Capotondi [d], L.G. Bellucci [d], D.D. Insinga [a], P. Petrosino [e], S. Bonomo [a], I. Cacho [f], A. Cascella [g], L. Ferraro [a], F. Florindo [h], C. Lubritto [i], P.C. Lurcock [h], D. Magri [c], N. Pelosi [a], R. Rettori [b], F. Lirer [a]

[a] Istituto per l'Ambiente Marino Costiero (IAMC), Consiglio Nazionale delle Ricerche, Calata Porta di Massa, Interno Porto di Napoli, 80133 Napoli, Italy
[b] Dipartimento di Fisica e Geologia, Università di Perugia, Via Alessandro Pascoli, 06123 Perugia, Italy
[c] Dipartimento di Biologia Ambientale Sapienza, Università di Roma, Piazzale Aldo Moro 5, 00185 Roma, Italy
[d] Istituto di Scienze Marine (ISMAR), Consiglio Nazionale delle Ricerche, Via Gobetti 101, 40129 Bologna, Italy
[e] DiSTAR — Dipartimento di Scienze della Terra, dell'Ambiente e delle Risorse, Università degli Studi di Napoli Federico II, Largo S. Marcellino 10, 80138 Napoli, Italy
[f] GRC Geociències Marines Dept. Estratigrafia, Paleontologia i Geociències Marines, Universitat de Barcelona, C/Martí Franques s/n, 08028 Barcelona, Spain
[g] Istituto Nazionale di Geofisica e Vulcanologia, Via della Faggiola 32, 52126 Pisa, Italy
[h] Istituto Nazionale di Geofisica e Vulcanologia, Via di Vigna Murata 605, 00143 Roma, Italy
[i] Dipartimento di Scienze e Tecnologie Ambientali Biologiche e Farmaceutiche (DiSTABiF), Seconda Università di Napoli, Via Vivaldi 47, Caserta, Italy

ARTICLE INFO

Article history:
Received 16 December 2015
Received in revised form 19 April 2016
Accepted 22 April 2016
Available online 30 April 2016

Keywords:
Planktonic foraminifera
Oxygen stable isotope
Pollen
Tephrostratigraphy
Magnetostratigraphy
Tyrrhenian Sea
Mediterranean Sea

ABSTRACT

We present a high-resolution paleoclimatic and paleoenvironmental reconstruction of the last five millennia from a shallow water marine sedimentary record from the central Tyrrhenian Sea (Gulf of Gaeta) using planktonic foraminifera, pollen, oxygen stable isotope, tephrostratigrapy and magnetostratigrapy. This multiproxy approach allows to evidence and characterize nine time intervals associated with archaeological/cultural periods: Eneolithic (base of the core–ca. 2410 BCE), Early Bronze Age (ca. 2410 BCE–ca. 1900 BCE), Middle Bronze Age–Iron Age (ca. 1900 BCE–ca. 500 BCE), Roman Period (ca. 500 BCE–ca. 550 CE), Dark Age (ca. 550 CE–ca. 860 CE), Medieval Climate Anomaly (ca. 860 CE–ca. 1250 CE), Little Ice Age (ca. 1250 CE–ca. 1850 CE), Industrial Period (ca. 1850 CE–ca. 1950 CE), Modern Warm Period (ca. 1950 CE–present day). The reconstructed climatic evolution in the investigated sedimentary succession is coherent with the short-term climate variability documented at the Mediterranean scale.
By integrating the planktonic foraminiferal turnover from carnivorous to herbivorous–opportunistic species, the oxygen isotope record and the pollen distribution, we document important modification from the onset of the Roman Period to the present-day. From ca. 500 CE upwards the documentation of the cooling trend punctuated by climate variability at secular scale evidenced by the short-term $\delta^{18}O$ is very detailed. We hypothesise that the present day warm conditions started from the end of cold Maunder event. Additionally, we provide that the North Atlantic Oscillation (NAO) directly affected the central Mediterranean region during the investigated time interval.

1. Introduction

Over the last millennia, the Mediterranean Sea was affected by very significant shifts in climate (i.e., Luterbacher et al., 2012; Maselli and Trincardi, 2013; Büntgen et al., 2016). The most common phases may be correlated with the major archaeological subdivisions found in the literature: Roman Period, Dark Age, Medieval Climate Anomaly and Little Ice Age (i.e., Luterbacher et al., 2012; Büntgen et al., 2016 and references therein).

However, it is worth noting the consensus, over the last two millennia, concerning the used and the chronology of terms Little Ice Age (LIA), Medieval Climate Anomaly (MCA) and Dark Age (i.e., Luterbacher et al., 2012 and references therein). This consensus is basically related to Pages 2k Network research activities (mostly tree ring data, i.e., Büntgen et al., 2016 and references therein). Recently, marine data also contributed to recognition of these events (i.e., Lirer et al., 2014; Holmgren et al., 2015; Cisneros et al., 2016). No agreement exists about the climatic variability during the second half (first 400 years CE) of the Roman Period (Table 1). In fact, despite of the data available for this part of the Roman Period (i.e., Moreno et al., 2012; Grauel et al., 2013; Lirer et al., 2014; Goudeau et al., 2015; Cisneros et al., 2016; Gogou et al., 2016), other factors as local overprint (i.e., Cisneros et al., 2016), a non-uniform response of climate signals among the various basins (Gogou et al., 2016) and the sensitivity of

* Corresponding author at: Istituto per l'Ambiente Marino Costiero (IAMC) - Consiglio Nazionale delle Ricerche, Calata Porta di Massa, Interno Porto di Napoli, 80133, Napoli, and Dipartimento di Fisica e Geologia - Università di Perugia, Via Alessandro Pascoli, 06123 Perugia, Italy.
E-mail address: giuliamargaritelli@hotmail.it (G. Margaritelli).

http://dx.doi.org/10.1016/j.gloplacha.2016.04.007
0921-8181/

Table 1
Table with ages and nomenclature of the climatic events documented in marine Mediterranean records for the last five millennia compared with the archaeological periods reported by Roberts et al. (2011). The acronym LBA corresponds to Late Bronze Age.

Nieto-Moreno et al. (2011)		Nieto Moreno et al. (2012)		Lirer et al. (2014)		Grauel et al. (2013)		Goudeau et al. (2015)		Piva et al. (2008a)		Gogou et al. (2012)		Roberts et al. (2011)	
West Algerian–Balearic basin		Western Alborean Sea		South Tyrrhenian Sea		Ionian Sea		Ionian Sea		Adriatic Sea		Aegean Sea		Italy	
Climatic phase	Ages	Climatic phase	Ages	Climatic phase	Ages	Climatic phase	Ages	Climatic phase	Ages	Climatic phase	Ages	Climatic phase	Ages	Achaeological Period	Ages
				Modern Warm Period	1940 CE–upwards			Present	1904 CE–1958 CE						
		Industrial Period	1800 CE–upwards	Industrial Period	1940 CE–1850 CE										
Little Ice Age	1800 CE–1300 CE	Little Ice Age	1800 CE–1300 CE	Little Ice Age	1850 CE–1240 CE	Little Ice Age	1850 CE1400 CE	Little Ice Age	1850 CE–1400 CE	Little Ice Age	1840 CE–1400 CE	Little Ice Age	1850 CE–1300 CE		
Medieval Classic Anomaly	1300 CE–800 CE	Medieval Classic Anomaly	1300 CE–800 CE	Medieval Classic Anomaly	1240 CE–840 CE	Medieval Warm Period	1200 CE–800 CE	Medieval Classic Anomaly	1200 CE — 800 CE	Medieval Warm Period	1200 CE–600 CE	Medieval Warm Period	1300 CE–900 CE		
Dark Age	800 CE–350 CE	Dark Age	800 CE–300 CE	Dark Age	840 CE–530 CE	Dark Age	750 CE–500 CE			Dark Age	600 CE–350 CE	Dark Age	900 CE–500 CE		
Roman Humid Period	350 CE–650 BCE	Roman Humid Period	300 CE–650 BCE	Roman period	Top–530 CE	Roman Warm Period	200 CE–1 CE	Roman Humid Period	450 BCE–0 CE	Roman Warm Period	350 CE–100–BCE	Roman Warm Period	500 CE–0 CE	Roman Period	Top–ca. 500 BCE
LBA/Iron Age	650 BCE–1650 BCE							Bronze Age	500 BCE–1500 BCE	Iron Age	ca. 100 BCE–1500 BCE			Greek–Etrurian	ca. 500 BCE–750 BCE
										Late Bronze Age	ca.1500 BCE–1850 BCE			Early Iron Age	ca. 750 BCE — 1050 BCE
										Ancient Bronze Age	ca.1850 BCE –2600 BCE			Late Bronze Age	ca.1050 BCE–1450 BCE
										Copper Age	ca.2600 BCE –2800 BCE			Middle Bronze	ca.1450 BCE–1750 BCE
														Early Bronze	ca.1750 BCE–2250 BCE

the biotic and abiotic proxies, can suggest different paleoclimatic interpretations (i.e., Roman Warm Period/Roman Humid Period). The climatic subdivision results more complicated for the last 3000 years BCE because this period has less chronological datasets.

The link between the most significant paleoenvironmental changes and the climate phases has been recently documented in different marine and continental archives (e.g., Piva et al., 2008a, 2008b; Jalut et al., 2009; Roberts et al., 2011; Lirer et al., 2014; Goudeau et al., 2015; Sadori et al., 2015; Gogou et al., 2016). These correlations are very useful to solve the land–sea interactions (synchronicity of proxy-events) and evaluate the impact of climate changes in societal organizations. In fact, recent studies (i.e. Magny et al., 2013; Holmgren et al., 2015; Sadori et al., 2015; Büntgen et al., 2016) suggested a continuous interaction between climate changes and the modifications of human societies and adaptive strategies.

The complicated land–sea interactions and the presence of steep mountain ridges close to the coast help to explain the spatial heterogeneity of climate in the Mediterranean region and represent a well-known problem for the correct simulation of its climate (Corte-Real et al., 1995; Lionello, 2012). However, it is largely accepted that the North Atlantic Oscillation (NAO), El Nino–Southern Oscillation (ENSO) and the Atlantic Multi-decadal Oscillation (AMO) represent the major factors in climate and oceanic variability in the Mediterranean region (Malanotte-Rizzoli et al., 2014 and reference therein). Previous research has also identified the NAO as one of the dominant atmospheric mode controlling the temporal evolution of precipitation and temperature in the Mediterranean area (López-Moreno et al., 2011) even if the interpretation of the NAO effect in the Mediterranean region is somewhat controversial, making crucial the need of fossil archive investigations. Planktonic foraminifera are commonly used as paleoenvironmental proxies in paleoceanographic investigations since they respond to changes of the environmental parameters of the water masses where they live (Bé and Tolderlund, 1971; Bé, 1977; Fairbanks and Wiebe, 1980; Hemleben et al., 1989; Ravelo et al., 1990; Le and Shackleton, 1994; Kucera et al., 2005). Furthermore, high-resolution studies performed in different basins of Mediterranean pointed out that the distributional pattern of some planktonic foraminiferal species are also useful for regional correlation (i.e., Sprovieri et al., 2003; Piva et al., 2008a; Budillon et al., 2009; Rouis-Zargouni et al., 2010; Lirer et al., 2013).

Within this framework, the high sedimentation rates characterizing the northern (Di Bella et al., 2014) and southern Tyrrhenian Sea (Budillon et al., 2005; Sacchi et al., 2009; Lirer et al., 2013, 2014), Gulf of Taranto (Grauel et al., 2013; Taricco et al., 2015; Goudeau et al., 2015) and Adriatic Sea (Oldfield et al., 2003; Piva et al., 2008a, 2008b), make the Mediterranean area an ideal archive to investigate paleoclimate changes at decadal and secular scale over the last millennia.

To contribute to a better understanding of late Holocene paleoclimate changes in the Mediterranean area, this work presents data collected in the central Tyrrhenian Sea (Gulf of Gaeta). We used planktonic foraminifera and pollen data with oxygen stable isotope signal.

Based on radionuclides analyses, tephrostratigraphy and oxygen isotope stratigraphy we offer a record at decadal time resolution. In addition, we provide the comparison of our data with the NAO index curve in order to document the link of the Mediterranean region with the North Atlantic climate change conditions.

2. Study area

The Mediterranean is an elongated and semi-enclosed basin, with an *anti*-estuarine circulation pattern forced by the negative hydrological balance and the density gradient with the Atlantic Ocean (Robinson and Golnaraghi, 1994) where evaporation exceeds precipitation (Bergamasco and Malanotte-Rizzoli, 2010). At Gibraltar, Atlantic water inflows in the surface layer with temperature $T = 15$ °C and salinity $S = 36.2$ psu and becomes Modified Atlantic Water (MAW) along its path to the Eastern basin. In the bottom layer Mediterranean water, the Levantine Intermediate Water (LIW) with $T = 13.5$ °C and $S = 38.4$‰ psu outflows. The transformation of MAW into LIW occurs through surface heat loss and evaporation specifically in the Levantine basin. Mediterranean has an overall resulting mean heat loss in the range of 3–7 W/m^2 (i.e., Bergamasco and Malanotte-Rizzoli, 2010).

The Tyrrhenian Sea is the deepest major basin in the western Mediterranean (Astraldi and Gasparini, 1994) and is connected to the other Mediterranean sub-basins through the Corsica Channel in the north and the Sardinia Channel in the south. The circulation is overall cyclonic triggered by the MAW entering off the northern Sicilian coast and establishing a northward current along the western Italian coast (Krivosheya and Ovchinnikov, 1973; Millot, 1987; Artale et al., 1994; Pierini and Simioli, 1998). According to De Pippo et al. (2003–2004) the circulation pattern of the Tyrrhenian Sea, which influences the Gulf of Gaeta, has a cyclonic vortex that interacts with the superficial (down to 10 m depth) and the intermediate (from 10 to 100 m depth) water layers (Bonomo et al., 2014).

The Gulf of Gaeta is also strongly influenced by the presence of the Volturno River, the longest river in southern Italy (175 km) with an estimated mean discharge of 40 m^3 s^{-1}, and a 1550 km^2 catchment basin (Iermano et al., 2012).

The continental shelf of the Gulf of Gaeta is the seaward extension of the Garigliano and Volturno coastal alluvial plains filled by Plio-Quaternary clastic and volcaniclastic deposits (de Alteriis et al., 2006); it is bounded by Cape Circeo to the north, Ischia and the Gulf of Naples to the south, and the Pontine Islands to the west; it narrows from NW to SE (from some tens of kilometres to kilometres north of Island Ischia) (de Alteriis et al., 2006).

3. Material and methods

3.1. Core lithology

The present study focused on the composite marine sequence of the core SW104-C5 (40°58′24,993″N, 13°47′03,040″E), 108 cm below the sea floor (cmbsf) length, and core C5 (40°58′24.953′N, 13°47′02,514″E), 710 cmbsf length, recovered in the Gulf of Gaeta, at 93 m water depths during the oceanographic cruise AMICA2013 (Fig. 1). The correlation between cores SW104-C5 and C5 is based on the identification of a Vesuvius tephra layer in the magnetic susceptibility record (Fig. 2) (see Section 4.2 for details). The studied interval (the first 452 cm composite depth) is characterized by light grey hemipelagic sediments (Fig. 2).

3.2. Planktonic foraminifera

Planktonic foraminiferal analysis was based on 346 samples collected at 1.3 cm spacing.

Samples were oven dried at 50 °C and washed using a 63 μm mesh sieve. Quantitative planktonic foraminiferal analysis was carried out on the fraction > 90 μm to avoid the juvenile specimens (Vallefuoco et al., 2012).

The main ecological interpretations used in this work follow, especially, Hemleben et al. (1989) and Pujol and Vergnaud Grazzini (1995) and are summarised in Table 2. Some planktonic species have been grouped as follows: *Orbulina* spp. includes *Orbulina universa* and *Orbulina suturalis*; *Globigerinoides quadrilobatus* includes *Globigerinoides trilobus*; *Globigerinoides ruber* includes *Globigerinoides gomitulus*; *Globigerina bulloides* includes *Globigerina falconensis*; *Globigerinella siphonifera* includes *Globigerinella calida*. Analysis discriminated also between left and right coiling of *Globorotalia truncatulinoides*, *Globorotalia inflata* and *Neogloboquadrina pachyderma*. Planktonic foraminiferal species are plotted in percentages of the total assemblage.

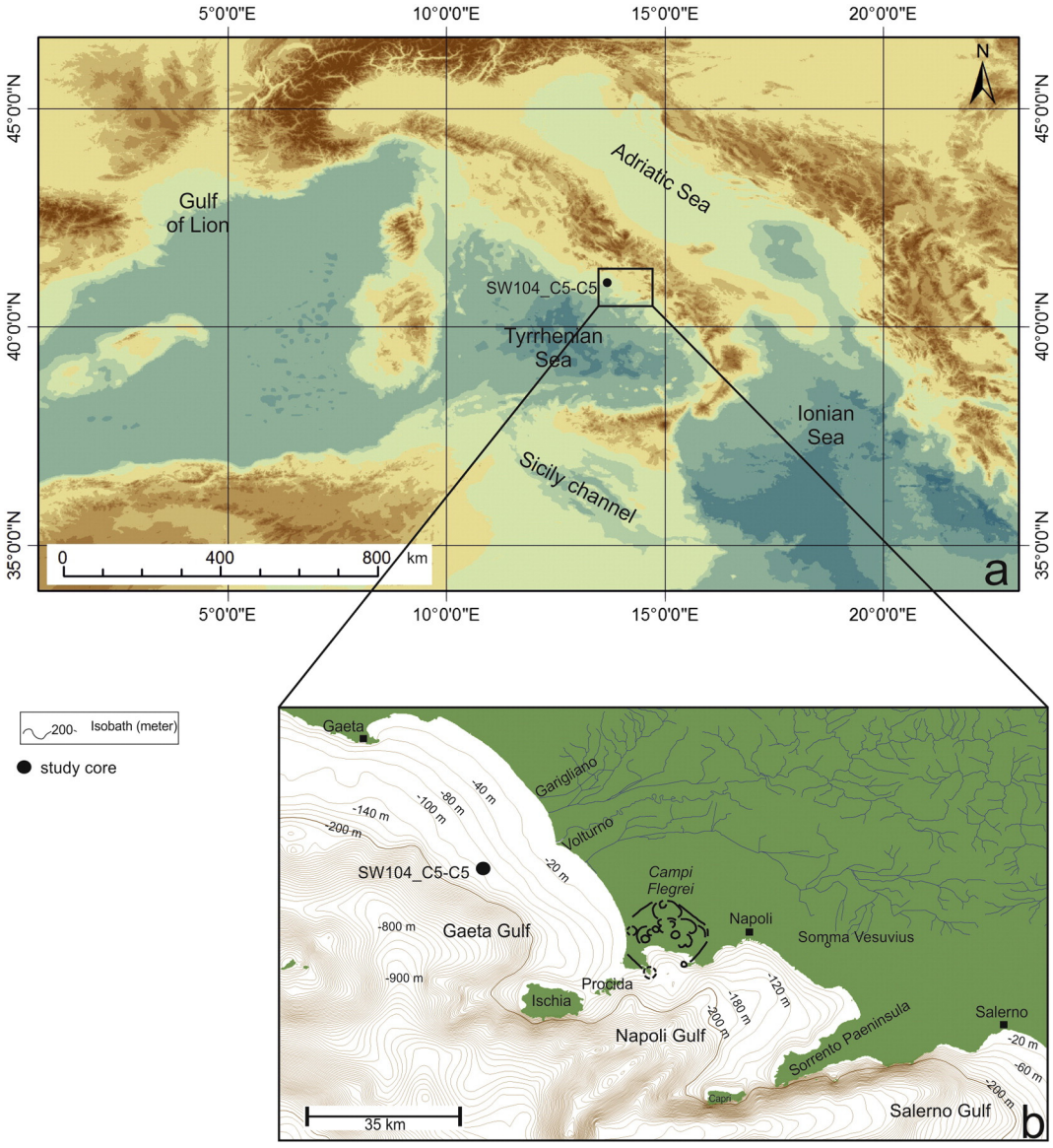

Fig. 1. (a): Location map of the study area; (b): bathymetric map of the study area with the location of the study core and the hydrographic grids of Garigliano and Volturno rivers.

Globorotalia scitula and *Neogloboquadrina pachyderma* were summed as indicators of cool water conditions; in particular, *G. scitula* is generally associated with cool water (Bé and Hutson, 1977; Hemleben et al., 1989), *N. pachyderma* is a deep-dwelling species living close to or below the thermocline (Capotondi et al., 2006). Also *G. glutinata* and *T. quinqueloba* are summed together in interpreted as proxy of the productivity in the sub- surface waters (Cita et al., 1977; Corselli et al., 2002; Geraga et al., 2008; Jonkers et al., 2010) (Table 2).

In order to characterize environmental changes we also plotted the distribution pattern of the herbivorous–opportunistic planktonic foraminiferal species (*T. quinqueloba*, *G. glutinata*, *G. bulloides*) and carnivorous ones (*G. ruber*, *G. quadrilobatus*, *Orbulina* spp., *G. siphonifera*) based on their ecological requirements reported in Table 2.

3.3. Radionuclides ^{210}Pb and ^{137}Cs

The chronology for the uppermost 60 cmbsf is based on sedimentation rate estimated by ^{210}Pb and ^{137}Cs. The ^{210}Pb and ^{137}Cs analysis were carried out at ISMAR-CNR Bologna, following the procedures reported in Bellucci et al. (2007). Alpha spectrometry of ^{210}Po was used for ^{210}Pb determinations, assuming secular equilibrium between the two isotopes. Supported ^{210}Pb activities were obtained from the constant values at depth in the core, where ^{210}Pb and ^{226}Ra were considered to be in radioactive equilibrium. Excess ^{210}Pb was calculated by subtracting the supported ^{210}Pb activity from the total ^{210}Pb activity.

The sediment accumulation rate was calculated using the constant flux–constant sedimentation model (CF–CS) (Sanchez-Cabeza and Ruiz-Fernández, 2012). To validate the ^{210}Pb-derived accumulation rates, ^{137}Cs activities were measured via gamma spectrometry using coaxial intrinsic Germanium detectors.

3.4. Magnetostratigraphy

As an additional check on the age model, a paleomagnetic inclination study was conducted using u-channel samples extracted from the centre of the C5 core and analysed at 1 cm intervals. Analysis was carried out at the INGV paleomagnetic laboratory in Rome. The u-channels were progressively demagnetized by alternating-field treatment at 5, 10, 15, 20, 25, 30, 40, 50, 60, 80, and 100 mT, and the remaining magnetization measured at each using a 2G Enterprises cryogenic magnetometer. The resulting demagnetization paths were analysed using the PuffinPlot software of Lurcock and Wilson (2012) to apply

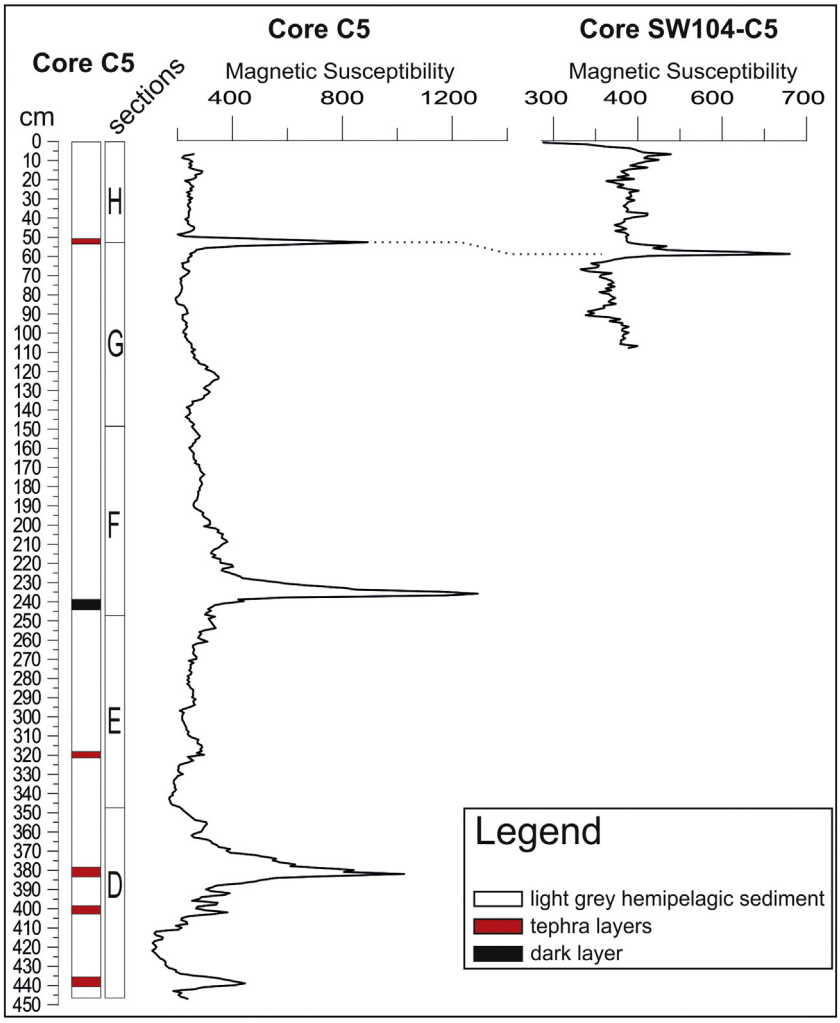

Fig. 2. From the left: Lithological log of core C5, magnetic susceptibility of C5 and SW104-C5 cores. The dotted black line represents the correlation point between the two study cores.

principal component analysis (Kirschvink, 1980), providing paleomagnetic inclination values for comparison with regional geomagnetic reference curves.

3.5. Oxygen stable isotope

Oxygen and Carbon isotope analyses were carried out on about ten specimens of the planktonic foraminiferal species *G. ruber* alba variety. Analyses were performed at the geochemistry laboratory of the IAMC-CNR (Naples, Italy) with an automated continuous flow carbonate preparation Gas BenchII device (Spötl and Vennemann, 2003) and a ThermoElectron Delta Plus XP mass spectrometer. Acidification of samples was performed at 50 °C. Every 6 samples, an internal standard (Carrara Marble with $\delta^{18}O = -2.43‰$ versus VPDB and $\delta^{13}C = 2.43‰$ vs. VPDB) was run and every 30 samples the NBS19 international standard was measured. Standard deviations of carbon and oxygen isotope measures were estimated at 0.1 and 0.08‰, respectively, on the basis of ~200 samples measured three times. All the isotope data are reported in δ‰ versus VPDB.

3.6. Pollen

Pollen analysis was carried out on 86 samples collected in the upper 480 cm of the SW104-C5–C5 composite core. They were chemically treated with HCl (37%), HF (40%) and NaOH (20%), following the standard procedure proposed by Fægri et al. (1989). Pollen concentration values were estimated by adding *Lycopodium* tablets to known weights of sediment (Stockmarr, 1971). Pollen grains were identified by means of a light microscope at 400 and 630 magnifications, with the help of both pollen morphology atlases (Reille, 1992, 1995, 1998; Beug, 2004) and the reference collection at the Laboratory of Palaeobotany and Palynology of Sapienza University of Rome. The main percentage sum is based on terrestrial pollen excluding pollen of aquatics and non-pollen palynomorphs (fungal and algal spores, as well as microscopic fragments of various organisms found in the pollen slides). Excluding aquatics, spores and other non-pollen palynomorphs (NPPs), an average number of ca. 200 pollen grains per sample were counted. These represent a statistically reliable number to undertake a reconstruction of the vegetation history, especially considering the low pollen concentrations (1300–7000 grains/g of sediment) and the fraction of analysed sample (often >10%).

The results of pollen analysis are presented as a summary diagram including: the record of total pollen concentration, the records of cumulative percentages of conifers (mostly represented by *Pinus*, *Juniperus*, and *Abies*), riparian trees (*Alnus*, *Salix*, *Populus*, and *Tamarix*), deciduous trees (mostly deciduous *Quercus*, *Corylus*, *Fagus*, *Ostrya*/*Carpinus orientalis*, *Carpinus betulus* and *Ulmus*), evergreen trees and shrubs (evergreen *Quercus*, Ericaceae, *Phillyrea*, and *Pistacia*), anthropogenic indicators (including *Castanea*, *Olea*, and other cultivated and anthropocore plants such as *Juglans*, *Vitis*, *cereals*, etc.), the record of Arboreal Pollen (AP) percentages. The group "other herbs" includes all the remaining herbaceous taxa. We decided to count *Olea* and *Castanea*

Table 2
Ecological requirements for planktonic foraminifera from literature data.

Species	Ecological preference	References
Turborotalita quinqueloba	Areas influenced by continental runoff	Cita et al. (1977), Corselli et al. (2002), Jonkers et al. (2010), Vallefuoco et al. (2012)
	Cold productivity surface waters; spring bloom	Cita et al. (1977), Corselli et al. (2002), Geraga et al. (2008), Jonkers et al. (2010)
Globigerinita glutinata	Areas influenced by continental runoff	Cita et al. (1977), Corselli et al. (2002), Jonkers et al. (2010), Vallefuoco et al. (2012)
	Productivity surface waters	Cita et al. (1977), Corselli et al. (2002), Geraga et al. (2008), Jonkers et al. (2010)
	Prevalence of cold, well-mixed, nutrient-rich waters in winter	Sprovieri et al. (2003)
	Opportunistic response to any increase in nutrient availability	Casford et al. (2002)
Globigerinoides ruber alba variety	Warm and oligotrophic surface waters (late summer-to early-winter)	Pujol and Vergnaud Grazzini (1995), Bàrcena et al. (2004)
Globigerinoides ruber pink variety	Wet conditions; warm surface waters	Piva et al. (2008a, 2008b)
Globigerinoides elongatus	Deepening of the summer thermocline during oligothophic conditions	Capotondi et al. (2016), Wang (2000), Numberger et al. (2009)
Globigerinoides quadrilobatus	Warm, low salinity, oligotrophic surface waters in summer	Hemleben et al. (1989), Pujol and Vergnaud Grazzini (1995)
	Mixed layer	Spooner et al. (2005)
Globigerinella siphonifera	Warm water taxa	Pujol and Vergnaud Grazzini (1995)
Globorotalia truncatulinoides	Prevalence of cold, well-mixed, nutrient-rich waters in winter	Sprovieri et al. (2003), Pujol and Vergnaud Grazzini (1995)
	Vertical mixing within the water column	Hemleben et al. (1989)
Globorotalia scitula	Low temperatures	Hemleben et al. (1989), Pujol and Vergnaud Grazzini (1995) and Sprovieri et al. (2003)
Neogloboquadrina pachyderma	Cold climatic condition	Hemleben et al. (1989), Pujol and Vergnaud Grazzini (1995) and Sprovieri et al. (2003)
	Deep-dwelling species living close to or below the thermocline; deep chlorophyll maximum at the base of the euphotic layer	Capotondi et al. (2006)
Orbulina spp.	Warm surface water	Pujol and Vergnaud Grazzini (1995)

in the anthropogenic indicator, instead of evergreen and deciduous trees respectively, because their trend in the pollen record seems mostly determined by human activity.

The distribution of the modern vegetation of the Gulf of Gaeta borderlands appears to be strongly related to both the inland orographic complexity and the vicinity of the sea, being influenced by insolation, altitude, moisture availability and soil (Blasi et al., 2014 for a recent bioclimatic classification of the area). *Sclerophyllous shrublands* and *Quercus ilex* woodlands generally dominate the coastal promontories and the south-facing slopes at low altitudes (ca. 0–600 m), while mixed evergreen/deciduous and deciduous forest formations are more frequent at higher altitudes, favoured by orographic humidity. In the limestone massif of the Ausoni and Aurunci mountains, for example, *Quercus pubescens* woodland is mostly distributed on the footslopes, whereas *Quercus cerris* woodland dominates the bottom of the intra-montane karst plateaus. The north facing slopes of these mountains are rich in *Carpinus orientalis* and *Ostrya carpinifolia* woods, located in the hilly and montane zone respectively. The highest altitudes of the montane zone are covered by *Fagus sylvatica* forests (Di Pietro, 2011). In the volcanic district of Roccamonfina, chestnut cultivations represent the main element of land cover (Catalano et al., 2010; Croce and Nazzaro, 2012). Conifer forests have a restricted patchy distribution in the land bordering the Gulf of Gaeta; including coastal and inland *Pinus* plantations (Croce and Nazzaro, 2012). The agricultural areas, with arable lands and permanent orchards and olive groves, extensively cover plains and foothill zones.

3.7. Tephrostratigraphic analysis

Tephra recognition was driven by the occurrence of peaks in magnetic susceptibility signal coupled to the inspection of washed sediments (>63 μm fraction) used for planktonic foraminifera analysis. Cryptotephra samples, used for chemical analyses, were labelled with C5 followed by an alphanumerical code pointing to the depth in cmbsf of the very base of the deposit (C5/53; C5/319; C5/403; C5/414 and C5/437).

For each sample, at least 30 juvenile fragments were then embedded in epoxy resin and suitably polished for microprobe analysis. In situ Energy Dispersive Spectrometric (EDS) analyses were performed on glass shards and loose minerals using JEOL JSM-5310 SEM at CISAG (Centro Interdipartimentale di Servizio per Analisi Geomineralogiche) of University of Federico II Napoli through Oxford Instruments Microanalysis Unit, equipped with an INCA X-act detector. Operating conditions were 15 kV primary beam voltage, 50–100 mA filament current, 50 s acquisition time with variable spot size. Correction for matrix effect was performed using INCA version 4.08 software that used the XPP correction routine, based on a Phi-Ro-Zeta approach. Primary calibration was performed using international mineral and glass standards USMN reference samples according to the following scheme: Anorthoclase 133,868 for Si and Na, Microcline 143,966 for Al and K, Fayalite 85,276 for Mn, Anorthite 137,041 for Ca, Hornblende 143,965 for Fe, Mg and Ti, Scapolite 6600–1 for Cl, Apatite 104,021 for P. Precision and accuracy were assessed using the rhyolitic glass USMN 75854 as secondary standard. Mean precision was <5% for SiO_2, Al_2O_3, K_2O, CaO and FeO, and around 10% for the other elements.

4. Chronology

4.1. Radionuclides ^{210}Pb and ^{137}Cs

The ^{210}Pb activity-profile in composite core SW104-C5-C5 records an exponential decline with depth (Fig. 3), suggesting a constant sedimentation accumulation in the topmost part of the core. Using this profile, the sedimentation rate was calculated back to 60 cmbsf, applying the CF–CS model (Sanchez-Cabeza and Ruiz-Fernández, 2012). A mean sedimentation accumulation rate of 0.46 cm/yr was obtained, defining an age of 1885 CE at 60 cm to the sediment surface (Fig. 3). The ^{137}Cs activity is low, as previously reported in the Gulf of Salerno by Vallefuoco et al. (2012), but shows a clear trend, detectable from 34.5 cmbsf (Fig. 3). The peaks at 30.5 cmbsf and at 23.5 cmbsf, associated with 1954 CE (first appearance of ^{137}Cs fallout from beginning of nuclear testing) and to 1963 CE (maximum ^{137}Cs fallout from nuclear testing), respectively, have been used as two independent tie-points for the construction of the age-depth profile (Fig. 3).

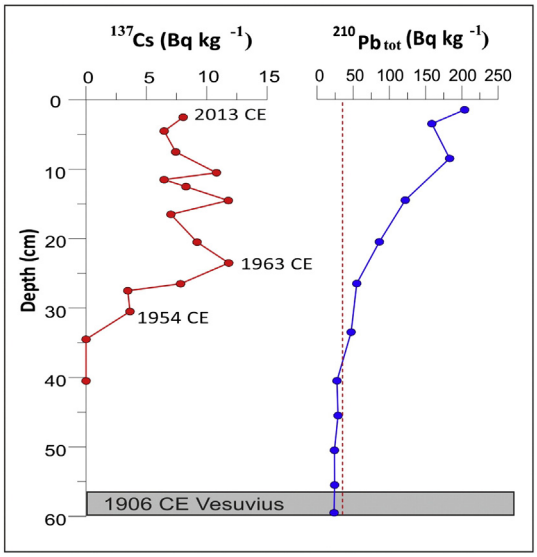

Fig. 3. Radionuclides analysis. ^{210}Pb and ^{137}Cs activity-depth profiles in core SW104-C5 with position of tie points. The grey band indicates the stratigraphic position (cmbsf) of the tephra layer associated to Vesuvius volcanic event 1906 CE (this work).

4.2. Tephrostratigraphy

Five cryptotephras were recognized along the record and they consist mainly of pumice, glass shard and minor scoria fragments, with rare lava lithic clasts and variable amounts of loose crystals. Three tephra layers (sampled at 437, 414 and 403 cmbsf), almost entirely made up of fresh glass, are interbedded within the stratigraphic interval from 437 cmbsf to 401 cmbsf mostly characterized by volcanic materials and minor bioclastic fragments, which suggest a continuous period of volcanoclastic input into the sedimentary system (Table 3).

The results of chemical analyses are reported in Table 4 as average values of individual point analyses for each sample recalculated to 100% water free. Individual chemical data points are given in Online Supplementary material. The analysed tephras have a wide range of composition ranging from phono-tephrites (tephra C5/53) to tephri-phonolites/latites (C5/319 and C5/414), trachytes and trachy-phonolites (C5/403, C5/414 and C5/437) according to TAS (total alkali/silica; Le Maitre, 2005) classification diagram (Fig. 4). Chemical features clearly indicate a provenance from the currently active volcanoes of the Neapolitan area (Ischia Island, Campi Flegrei, and Vesuvius).

4.2.1. Tephra C5/58

This is the youngest pyroclastic deposit, found in the core between 57 and 58 cmbsf. Its lithological features and the occurrence of leucite bearing scoriae, phono-tephritic in composition, are typical of Somma–Vesuvius deposits younger than 79 CE (Santacroce et al., 2008). Stratigraphy, ^{210}Pb and ^{137}Cs results clearly indicate for this tephra layer an emplacement slightly younger than 1885 CE (see above). Taking into account this chronological constrain along with the good chemical match between the studied sample and proximal deposits (Table 4), we relate tephra C5/58 to the 1906 eruption, the final phase of which produced fine ash fragments singularly spread towards the west of the volcano (Mastrolorenzo et al., 1993; Barsotti et al., 2015) and possibly affecting the core site area. The occurrence of these deposits in the Gaeta Bay represents the first finding of the post-1631 Vesuvius products in marine settings north of Naples Bay.

4.2.2. Tephra C5/319

The composition of glasses straddles the boundary between latites and tephri-phonolites (Fig. 4). They show a TiO_2 content mostly exceeding 0.8%, which represents a threshold that discriminates latites erupted at Ischia Island from those erupted at Campi Flegrei (CF) in the last 4000 years (Fig. 5). Few analytical points display high Al_2O_3 values (ca. 20%) for these types of rocks (Table 4) and this chemical feature was recently reported by D'Antonio et al. (2013) for a number of latitic deposits outcropping on the island. During the last 4000 years several close in time low VEI events took place with a dispersal area of products restricted to in narrow sectors around the vent (de Vita et al., 2010). Among them, the Vateliero eruption (VI–IV cent. BC, Table 3), occurred in the south-eastern sector of Ischia, was characterized by a sustained column phase emplacing a well sorted pumice fallout with a maximum thickness of 1 m in the vent area (Unit EUB2; de Vita et al., 2010). The good chemical match between tephra C5/319 and the glass fractions of the Vateliero deposits (D'Antonio et al., 2013), allows us to infer this land–sea correlation (Table 4). This correlation is also supported by the recognition in the study core of this tephra layer just above the acme end of *G. quadrilobatus* (see paragraph 4.3), dated at 2.7 ka BP by Lirer et al. (2013). As for the 1906 tephra, the occurrence of tephra C5/319 at this site represents the first finding of Vateliero products in a marine setting, thus enlarging the previously known dispersal.

4.2.3. Tephra C5/403, C5/414, C5/437

Glass fragments of tephras C5/403 define two slightly different compositions in the phonolite field, tephra C5/414 has a bimodal composition since it associates a minor tephri-phonolitic/latitic population to the prevailing trachy-phonolitic one, and C5/437 shows a homogeneous

Table 3
Summary of tephra layers analysed in the last five ka record of composite core SW104-C5–C5 (Gulf of Gaeta). a: age datum based on archaeological remains (de Vita et al., 2010); b: age datum from paleomagnetic measurements (Vezzoli et al., 2009); c: ^{40}Ar/^{39}Ar age (Di Renzo et al., 2011); d: ^{14}C calibrated age (Sacchi et al., 2014); e: modelled best age (Smith et al., 2011).

Tephra	Lithology	Thickness (cm)	Composition	Source	Eruption/Age
C5/58	Dark grey leucite bearing scoriae, loose crystals of feldspar and clinopyroxenes.	8	Tephri-phonolite	Vesuvius	1906 CE
C5/319	Micropumices and pumiceous glass shards, obsidians, loose crystals of feldspar, clinopyroxenes and biotite.	4	Trachyte/tephri-phonolite/latite	Ischia	Vateliero/VI–IV cent. B.C.[a] 800–620 BCE[b]
C5/403	Micropumices, obsidians, loose crystals of feldspars and clinopyroxenes.	3	Trachy-phonolite	Campi Flegrei	Capo Miseno?/3700 ± 500 years[c] 3904 ± 60 years[d]-Astroni 6?/4297–4192[e]
C5/414	Elongated glass shards and micropumices.	1	Trachy-phonolite-trachyte/latite	Campi Flegrei	Astroni 3/4098–4297 years BP[e]
C5/437	Light micropumices, brown blocky and pumiceous glass shards, loose crystals of feldspar, clinopyroxenes and biotite. Lithics and bioclasts.	~14	Trachy-phonolite	Campi Flegrei	Agnano Monte Spina/4482–4625 years BP[e]

Table 4
Averages and standard deviations of the major-element composition of composite core SW-104-C5–C5 tephras and their proximal equivalents discussed in the text. All analyses recalculated water-free to 100%. Total Fe expressed as FeO. Abbreviation: av. is the number of analyses considered for the average (bold); s.d. is standard deviation (italics). Source of data used for comparison: (1906) this study; (Vateliero) D'Antonio et al. (2013); (Capo Miseno) this study; (Astroni3, Astroni6 and Agnano Monte Spina -AMS) Smith et al. (2011).

Tephra sample	C5/58		Vesuvius 1906		C5/319 Comp. A		Ischia Vateliero		C5/319 Comp. B		C5/403 Comp. A		Campi Flegrei Capo Miseno		Campi Flegrei Astroni6		C5/403 Comp. B		Campi Flegrei Astroni6	
	av. 14	s.d.	av. 13	s.d.	av. 19	s.d.	av. 2	s.d.	av. 3	s.d.	av. 16	s.d.	av. 16	s.d.	av. 75	s.d.	av. 4	s.d.	av. 36	s.d.
SiO_2	46.76	0.67	47.46	0.77	56.15	0.71	57.77	0.27	56.23	0.64	59.99	0.48	59.15	0.39	60.17	0.42	58.32	0.45	58.98	0.27
TiO_2	1.28	0.16	1.33	0.23	1.04	0.22	1.10	0.17	0.86	0.22	0.42	0.15	0.44	0.18	0.46	0.04	0.51	0.21	0.52	0.03
Al_2O_3	17.99	0.34	17.58	0.52	18.43	0.26	18.44	0.08	21.07	0.30	18.83	0.29	18.93	0.32	19.01	0.23	19.03	0.21	19.05	0.14
FeO	10.20	0.76	10.27	0.56	5.70	0.39	5.38	0.11	4.10	0.50	3.61	0.28	3.50	0.43	3.48	0.17	4.35	0.37	4.03	0.14
MnO	0.19	0.16	0.32	0.15	0.13	0.11	0.19	0.01	0.14	0.12	0.12	0.12	0.14	0.15	0.14	0.04	0.13	0.16	0.13	0.04
MgO	3.12	0.31	3.48	0.47	1.63	0.17	1.38	0.31	1.11	0.20	0.63	0.09	0.56	0.08	0.61	0.05	0.78	0.14	0.89	0.14
CaO	8.77	0.34	8.95	0.64	4.48	0.48	3.53	0.45	6.04	1.10	2.85	0.30	2.67	0.17	2.55	0.12	3.23	0.18	3.21	0.17
Na_2O	4.90	0.27	4.10	0.38	4.48	0.14	4.74	0.16	4.49	0.23	4.49	0.25	4.46	0.29	4.56	0.20	4.20	0.13	4.11	0.13
K_2O	4.95	0.58	5.06	0.50	6.95	0.29	6.75	1.02	5.29	0.49	8.92	0.26	9.27	0.32	9.00	0.26	8.85	0.28	9.07	0.06
P_2O_5	1.05	0.24	0.88	0.14	0.64	0.29	0.38	0.03	0.42	0.18	0.14	0.11	0.21	0.13	0.10	0.02	0.60	0.10	0.20	0.02
Cl	0.79	0.12	0.57	0.16	0.38	0.05	0.35	0.06	0.27	0.03	0.60	0.48	0.69	0.07	0.74	0.06	0.51	0.07	0.52	0.02
Total	100.00		100.00		100.00		100.00		100.00		100.00		100.00		100.00		100.00		100.00	
Alkalis	9.85		9.16		11.43		11.49		9.78		13.41		13.37		13.56		13.05		13.18	
CaO + MgO	11.89		12.43		6.11		5.91		7.15		3.48		3.23		3.16		4.11		4.10	
K_2O/Na_2O	1.01		1.23		1.55		1.42		1.18		1.98		2.07		1.97		2.10		2.20	

Tephra sample	C5/414 Comp. A		Campi Flegrei Astroni3		C5/414 Comp. B		Campi Flegrei Astroni3		C5/437		Campi Flegrei AMS	
	av. 17	s.d.	av. 27	s.d.	av. 11	s.d.	av. 11	s.d.	av. 34	s.d.	av. 188	s.d.
SiO_2	60.65	0.66	60.58	0.34	56.70	0.89	57.40	0.23	60.50	0.63	60.45	0.56
TiO_2	0.56	0.12	0.46	0.03	0.61	0.09	0.72	0.04	0.49	0.18	0.48	0.04
Al_2O_3	18.47	0.24	19.13	0.21	18.44	0.29	17.95	0.14	18.49	0.26	18.73	0.23
FeO	3.12	0.32	3.44	0.22	5.29	0.47	5.55	0.18	3.49	0.32	3.65	0.26
MnO	0.20	0.13	0.15	0.04	0.17	0.13	0.14	0.05	0.14	0.12	0.14	0.04
MgO	0.53	0.13	0.54	0.04	1.52	0.31	1.67	0.06	0.57	0.10	0.70	0.12
CaO	2.69	0.46	2.40	0.07	4.87	0.59	4.08	0.08	2.46	0.22	2.67	0.26
Na_2O	4.01	0.48	4.51	0.26	3.26	0.16	3.48	0.11	4.38	0.32	4.28	0.35
K_2O	9.06	0.26	8.74	0.19	8.45	0.55	8.04	0.10	8.64	0.33	8.86	0.30
P_2O_5	0.04	0.07	0.79	0.06	0.16	0.21	0.56	0.03	0.11	0.10	0.63	0.07
Cl	0.68	0.14	0.10	0.04	0.52	0.07	0.40	0.02	0.73	0.12	0.12	0.03
Total	100.00		100.00		100.00		100.00		100.00		100.00	
Alkalis	13.07		13.25		12.71		11.52		13.02		13.14	
CaO + MgO	3.22		2.94		5.39		5.75		3.03		3.37	
K_2O/Na_2O	2.25		1.93		2.59		1.56		1.97		2.07	

trachy-phonolitic composition (Fig. 4). Chemical features of the analysed tephras are typical of Campi Flegrei (CF) products erupted during the last 5000 years (Smith et al., 2011). In particular, the bimodality of tephra C5/414 allows us to correlate this deposit to the Astroni3 event (Table 4) which is the only terrestrial counterpart showing such a peculiar chemistry for that time period (Smith et al., 2011). Taking into account this strong chemistry-supported correlation, the Astroni3 tephra can be considered a good chronological marker in the studied succession at 4098–4297 years BP (Smith et al., 2011) and it helps to temporally constrain tephras C5/403 and C5/437, which are otherwise characterized by a barely distinguishable glass chemistry.

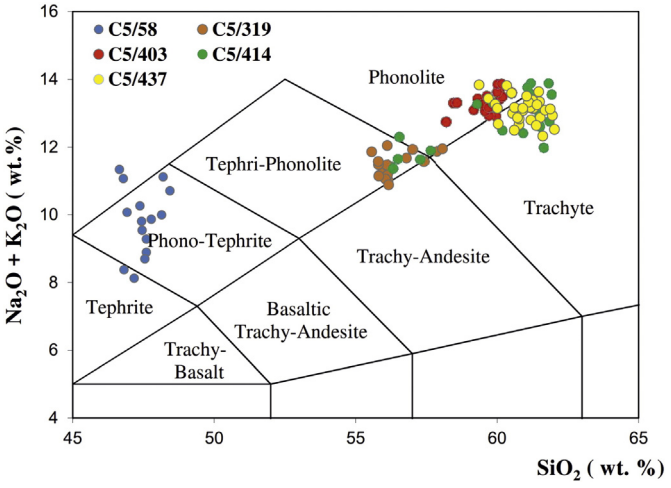

Fig. 4. Classification of the studied samples representative of tephra from core C5 according to the TAS (total alkali/silica diagram; Le Maitre, 2005).

In order to find a possible counterpart for tephra C5/403, we set its chemistry against that of Campi Flegrei deposits younger than Astroni3 and, according to SiO_2 *vs* CaO variation diagram, a tentative correlation could be proposed with Astroni6 products (4297–4192 years BP, Smith et al., 2011) characterized by a comparable large variability (Fig. 6a). However, the modelled age for tephra C5/403 ranges from ca. 3939 years BP to 4100 years BP (see Section 4.3) in good agreement also with the age of Capo Miseno event obtained from both proximal (3700 ± 500 years; Di Renzo et al., 2011) and offshore (3904 ± 60 cal. years BP; Sacchi et al., 2014) deposits. Moreover, the most representative chemical composition of C5/403 (16 out of 20 individual point data) is also well comparable to the chemistry of Capo Miseno glasses (Table 4). The co-occurrence of this tephra layer with the base of *G. quadrilobatus* acme event (see Section 4.3), dated at 3.7 ka BP (Lirer et al., 2013), strongly supports the correlation with Capo Miseno event.

Tephra C5/437 (9 cm below Astroni3) is the most prominent along the record and characterized by a large amount of fresh glass with different morphologies (Table 3). In the SiO_2 vs CaO variation diagram we compared its composition with that of Astroni1 and Agnano Monte Spina (4153–4345 years BP and 4482–4625 years BP,

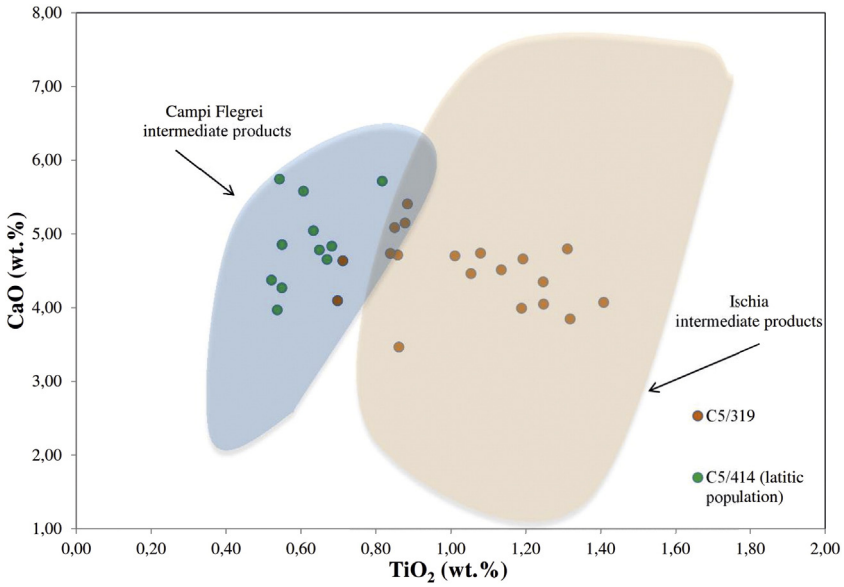

Fig. 5. TiO_2 vs. CaO diagram of tephras C5/319 and C5/414 found in core C5. The average compositional field of latitic products from Ischia and Campi Flegrei erupted in the last 4 ka are reported for comparison.
Data from: (CF) Smith et al. (2011); (Ischia) D'Antonio et al. (2013).

respectively; Smith et al., 2011) glasses and a fair agreement can be observed with the latter ones (Fig. 6b). Lithology and thickness (~14 cm) of the deposit support the correlation of tephra C5/437 with the eruption of Agnano Monte Spina (AMS) which represents the highest magnitude event of this time span. The correlation of this tephra with the AMS volcanic deposits is also supported by the occurrence in the study core of this tephra layer just above the strong drop in abundance of *G. truncatulinoides* left coiled (Fig. 7) dated at 4.5 ka BP by Lirer et al. (2013).

The products of the AMS eruption have been recently found in the Salerno Bay (Amato et al., 2012; Lirer et al., 2013), although they are mainly spread towards the eastern sector of the volcano (de Vita et al., 1999) and frequently found in the marine archives of the Adriatic Sea (Zanchetta et al., 2011 and references therein).

4.3. Age model

The age model has been constructed starting from radionuclides ages (^{210}Pb activity-depth profile and ^{137}Cs activity) for the last ca. 150 years and tephrostratigraphy of five tephra layers recorded in the study core [Vesuvius (1906 CE), Vateliero–Ischia (2.4–2.6 ka BP), Capo Miseno (3.7-3.9 ka BP), Astroni3 (4.1–4.3 ka BP), Agnano M. Spina (4.42 ka BP)] (Table 5). In addition we considered the following planktonic foraminiferal events: i) the abundance peak of *Globorotalia truncatulinoides* left coiled (1718 ± 10 yr CE, Lirer et al., 2013, 2014); ii) the acme interval of *G. quadrilobatus*, (base 3.7 ± 0.048 ka BP top 2.7 ± 0.048 ka BP, Lirer et al., 2013) (Table 5). These bioevents are documented in the different basins of the Mediterranean Sea and well time-constrained (Sprovieri et al., 2003; Di Bella et al., 2014; Cisneros et al., 2016). The chronology of the stratigraphic interval between the acme base of *G. truncatulinoides* left coiled and the top of *G. quadrilobatus* acme interval, has been obtained thought the tuning of the $\delta^{18}O_{G.\ ruber}$ record with the same signal from core C90 (Gulf of Salerno, south Tyrrhenian Sea, Lirer et al., 2013, 2014) (Fig. 7). The good visual comparison between the $\delta^{18}O_{G.\ ruber}$ signal from the study site (with data from south Tyrrhenian Sea (Lirer et al., 2013, 2014), Gulf of Taranto (Grauel et al., 2013) and eastern Mediterranean (Schilman et al., 2011) (Fig. 8) increases our confidence on the robustness of our age model. Linear interpolation between the tie-points used for constructing of the age-depth profile shows a progressive decrease in sedimentation rate from the top down to the base core (Fig. 7).

4.4. Magnetostratigraphy

The paleomagnetic inclinations were used to confirm the age model by comparison with a reference curve. In the absence of a sufficiently detailed reference curve for Italy or the Tyrrhenian Sea, we used data generated for the sampling location by the SHA.DIF.14k model of Pavón-Carrasco et al. (2014). The temporal resolution of the geomagnetic model is lower than that of our data, but sufficient to check the age model on centennial and longer time scales.

We conducted the comparison by using the age tie points listed in Table 5, and tuning the age-depth transformation between the tie-points using the Match software of Lisiecki and Lisiecki (2002). The age-inclination curve for Core C5 is shown in Fig. 9, with the reference curve included for comparison. The uppermost 60 cm of the core are omitted from this analysis, since the sediment was too liquid for reliable paleomagnetic measurement; soft sediment deformation is probably also responsible for the abnormally low inclination near the top of the measured core. There is good agreement between the major features of C5 inclination record and the reference curve, confirming the strength of the constructed chronology. Slight divergences can be explained in part by limitations on the accuracy of the model data at this location.

5. Results

5.1. Oxygen isotope analysis

The oxygen isotope signal measured out on the planktonic foraminiferal species *G. ruber* alba variety, from the last five millennia varies between 0.87‰ to −1.91‰ with a mean value of −0.12‰ (Fig. 10). $\delta^{18}O_{G.\ ruber}$ signal shows from the base of the core up to 200 CE a gentle shift from 0.86‰ to 0.12‰ (Fig. 10). This long interval is characterized by five distinct lower $\delta^{18}O_{G.\ ruber}$ values centred at 2600 BCE, 1800 BCE, 1600 BCE, 1400 BCE, and 1200 BCE (Fig. 10).

During the last two millennia, $\delta^{18}O_{G.\ ruber}$ signal shows an increase in frequency and amplitude oscillations with respect to the previous three

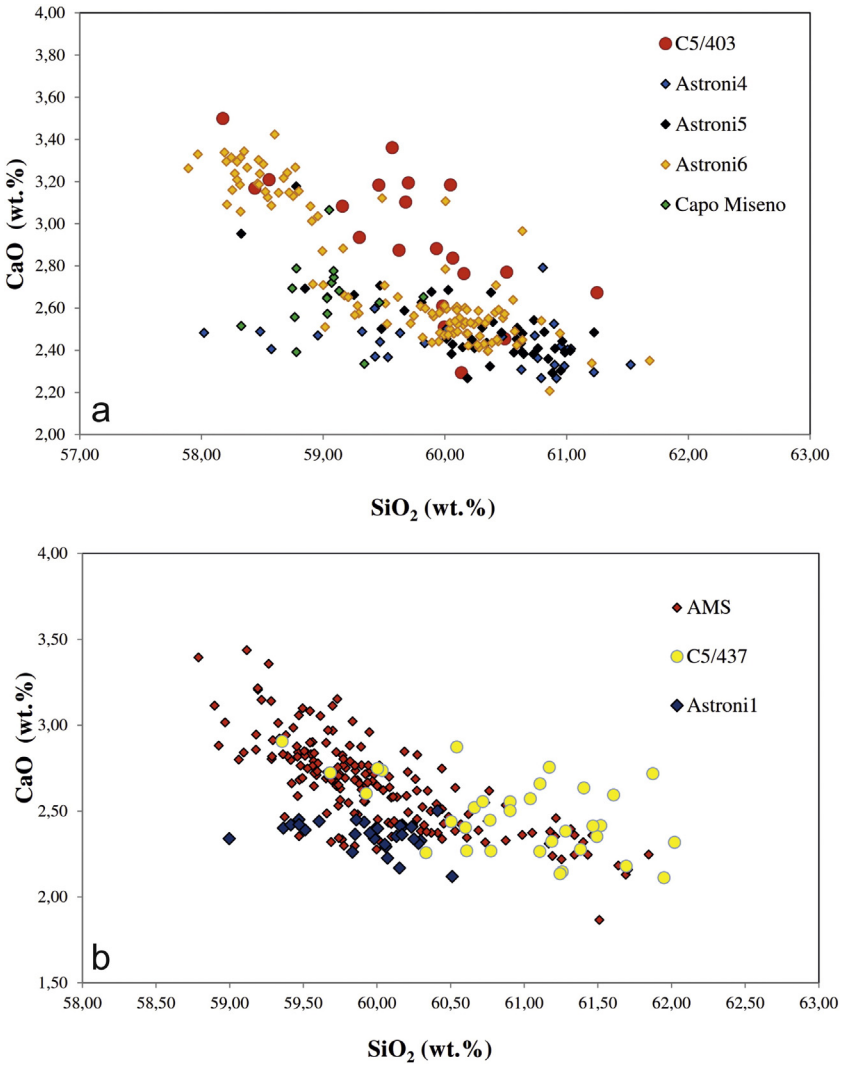

Fig. 6. a) SiO_2 vs CaO variation diagram for C5/403 tephra. The compositions of possible proximal counterparts from CF are reported for comparison. Data from: (Astroni 4–5–6) Smith et al., 2011; (Capo Miseno), this study (Supplementary Materials) b) SiO_2 *vs* CaO variation diagram for tephra C5/437. The compositions of possible proximal counterpart from CF are reported for comparison.
Data from Smith et al. (2011).

millennia BC (Fig. 10). In particular, high $\delta^{18}O_{G.\ ruber}$ values (mean values of 0.5‰) are documented at 500 CE and 800 CE, between 1300–1600 CE and 1700–1800 CE and at 1900 CE (Fig. 10). Low $\delta^{18}O_{G.\ ruber}$ values (mean values of −0.5‰) are detected at 350 CE, 600 CE, 1200 CE, 1650 CE, and at 1850 CE (mean values of −1‰), and at 1980 CE (mean values of −1.5‰) (Fig. 10).

5.2. Planktonic foraminifera

Planktonic foraminifera are abundant, well preserved and with mostly a very thin test. *G. ruber* alba and *G. elongatus* show a progressive decreasing trends from base core to 400 CE (Fig. 10). Upwards, *G. elongatus* is still present to 1550 CE (Fig. 10) with very low abundance (<2%), while from 1550 CE to present day it is almost absent (Fig. 10). Conversely, *G. ruber* alba shows two increasing trends, one starts at 400 CE and a second one at 1550 CE (Fig. 10). The onset of this latter abrupt increase in abundance (from 20 to 70%) fits with the virtual absence of *G. elongatus* (Fig. 10).

T. quinqueloba and *G. glutinata* display a progressive increase in abundance to ca. 1650 CE. From 1650 CE to 1900 CE, these taxa show a strong decrease in abundance while in the uppermost part of the core (from ca. 1900 CE to present day) they go through a significant percentage increase up to 60% (Fig. 10). *G. quadrilobatus* shows a peak in frequency from 700 BCE to ca. 1750 BCE reaching percentages of 25% (Fig. 10).

The other planktonic foraminiferal species show percentages ranging between 0.1 and 25% and only occasionally reached significant frequencies. *G. ruber* pink variety, *G. truncatulinoides* and *G. inflata* left coiled have a scattered distribution pattern and they are continuously present only from ca. 350 CE to present day. It is noteworthy the significant peak in percentage of *G. truncatulinoides* (17%) and *G. inflata* left coiled (5%) during the Maunder phase (Fig. 10).

G. siphonifera and *Orbulina* spp. are present with low percentages along the core and occasionally shows distinct peaks in frequency (Fig. 10). *G. scitula* and *N. pachyderma* right coiled group generally show very low percentages through the entire investigated interval. (Fig. 10).

5.3. Pollen analysis

The main vegetation features profiled by the pollen record over the last 5000 years suggest a landscape characterized by mixed evergreen and deciduous oak-dominated woodlands, showing major changes in both structure and floristic composition (Fig. 11).

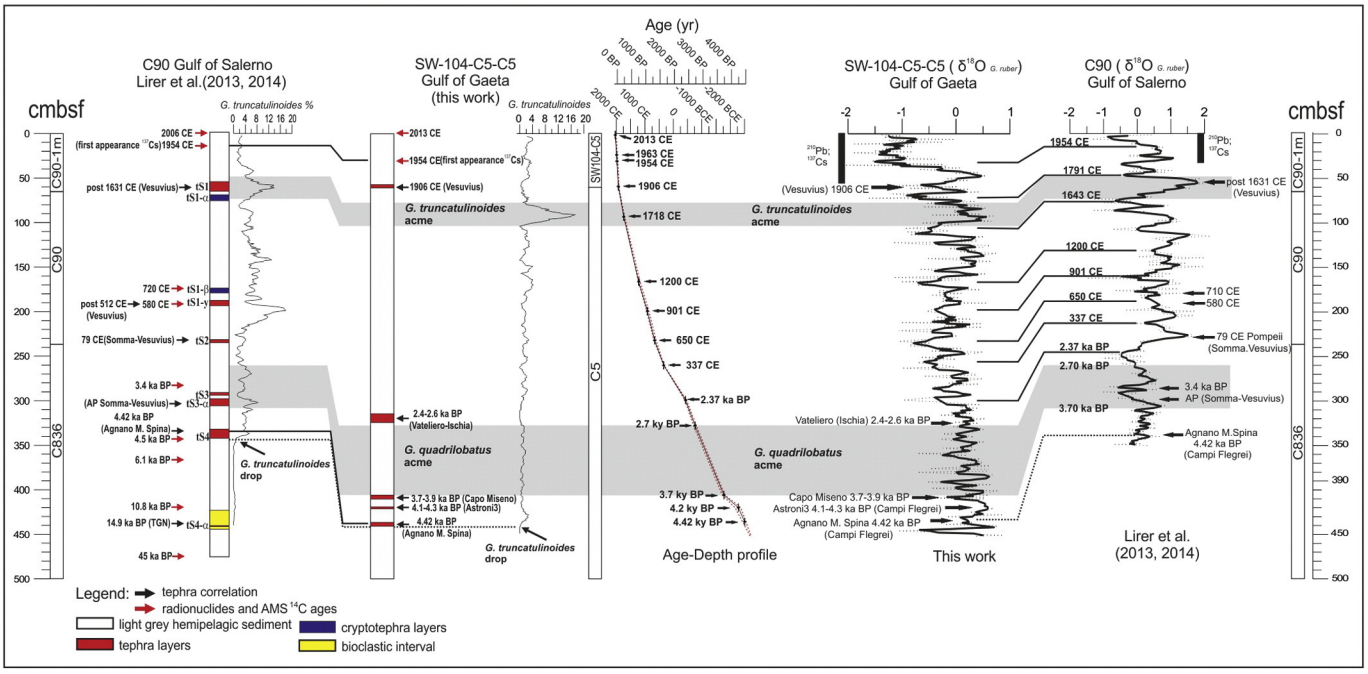

Fig. 7. From left side. Correlation between the composite core from Salerno Gulf (Lirer et al., 2013, 2014) and the composite core SW104-C5–C5 (Gulf of Gaeta, this work), based as follows: a) the first appearance of ^{137}Cs; b) the micropaleontological events represented by the acme intervals of *G. truncatulinoides* and of *G. quadrilobatus* (grey bands), and the drop in abundance of *G. truncatulinoides*; c) tephra layer associated to Agnano M. Spina volcanic event and d) $\delta^{18}O_{G.\ ruber}$ patterns. In the middle: Age depth profile of composite core SW104-C5–C5 (Gulf of Gaeta) with position of the tie-points used to calculate the sedimentation rate. The two red dotted lines represent the propagation of errors.

Between 3000 and 900 cal. BCE (Fig. 11) the forest composition shows the prevalence of evergreen elements, recorded in high frequencies (>45%). Between 900 and 100 cal. BCE a clear decrease in evergreen trees and shrubs is accompanied by an increase in herbs (max. 46%), enriched by xeric taxa like *Artemisia*, thus indicating an opening of the forest vegetation (Fig. 11). During the last two millennia, a fluctuating trend of broadleaved trees is recorded. The forest cover expanded, between ca. 100 BCE and 800 CE, mostly due to a general increase in deciduous taxa (up to 42%), while after 800 CE the landscape experienced a major new opening, resulting from a clear increase in herbaceous taxa and a further decline of broadleaved trees, especially evergreen taxa (Fig. 11). In particular, the AP pollen record shows two forest drops, from 800 to 1100 CE and from 1600 and 1850 CE, intermixed by a new moderate increase in arboreal vegetation from 1100 to 1600 CE (Fig. 11). Finally, the last two centuries are characterized by a new arboreal vegetation expansion (67%), mostly related to an increase in conifers dominated by *Pinus* (Fig. 11). This last time interval is also marked by high frequencies of anthropogenic pollen indicators (up to 24%), highlighting an undeniable influence exerted by human activities on the natural environment (Fig. 11).

6. Discussion

6.1. Paleoenvironmental reconstruction in the central Tyrrhenian Sea

An integrated dataset based on planktonic foraminifera, pollen, tephrostratigrahy and oxygen isotopes analysis performed on a marine sediment core collected in the central Tyrrhenian Sea allows identifying nine paleoclimatic intervals during the past five millennia, with decadal resolution. Based on our age model, these intervals correspond to the recent archaeological/cultural periods: Eneolithic, Early Bronze Age, Middle Bronze Age–Iron Age, Roman Period, Dark Age, Medieval Climatic Anomaly, Little Ice Age, Industrial Period and Modern Warm Period (Figs. 10, 11).

6.1.1. Eneolithic: base of the core to ca. 2410 BCE/base core–ca. 4360 BP

Generally warm-water conditions dominate during this interval as documented by the high percentages in frequency of *G. ruber* alba, *G. elongatus* and *Orbulina* spp.

$\delta^{18}O_{G\ .ruber}$ values associated with maximum abundance of *G. elongatus* evidence an increase in temperatures at ca. 2600 BCE (Fig. 10). In addition, the strong decrease in frequency of *T. quinqueloba* and *G. glutinata*, assumed as proxies of seasonal flooding events (Vallefuoco et al., 2012), suggests an environment setting with a reduced river runoff. Our reconstruction is in agreement with the paleoenvironmental scenario proposed by Piva et al. (2008a,b) in the Adriatic Sea at time of the warm event W4-Copper Age.

The pollen record documents a slight and slow opening of the forest vegetation especially in the broadleaved evergreen taxa (Fig. 11), suggesting a progressive establishment of a more arid climate in the third millennium BC (Di Rita and Magri, 2012).

6.1.2. Early Bronze Age: ca. 2410 BCE to ca. 1900 BCE/ca. 4360 BP–ca. 3850 BP

The beginning of the Early Bronze Age at ca. 2410 BCE (Fig. 10) corresponds to a turnover between carnivorous and herbivorous–opportunistic planktonic foraminifera marks.

The high abundance of *G. ruber*, *G. siphonifera* and *G. elongatus* in the lower part of this interval until ca. 2400 BCE reflects warm summer conditions (Fig. 10). The highest frequencies of *G. ruber* in the Mediterranean are generally reported at the end of the summer (Pujol and Vergnaud Grazzini, 1995) or in fall (Bàrcena et al., 2004). At the same time, the occurrence of *G. truncatulinoides* and *G. glutinata* (Fig. 10) suggests the prevalence of cold, well-mixed, nutrient-rich waters in winter (Sprovieri et al., 2003). A similar climatic reconstruction was reported in the Adriatic Sea and in the north-eastern Ionian Sea (Piva et al., 2008a,b; Geraga et al., 2008) evidencing an atmospheric connection among the different basins of the Mediterranean Sea.

From ca. 2300 BCE to ca. 2050 BCE, a strong increase in *T. quinqueloba* abundance, associated with the $\delta^{18}O_{G.ruber}$ signal enrichment (from 0‰

Table 5
List of the tie-points used for the construction of the age model of composite core SW-104-C5-C5 (Gulf of Gaeta).

Tie-points	depth (cm)	Age (CE/BCE)	Age (yr BP)	Error bar (years)	References
Top core	1	2013	−63	0	This work
Maximum ^{137}Cs fallout	23.5	1963	−13	2	This work
Beginning nuclear activity	30.5	1954	0	2	This work
Vesuvius (tephra layer)	58	1906	44	0	This work
Abundance peak of *Globorotalia truncatulinoides*	93	1718	232	10	Lirer et al. (2014)
Graphic correlation $\delta^{18}O_{G.\ ruber}$ with C 90 isotope record	166	1200	540	30	Lirer et al. (2014)
Graphic correlation $\delta^{18}O_{G.\ ruber}$ with C 90 isotope record	199	901	750	38	Lirer et al. (2014)
Graphic correlation $\delta^{18}O_{G.\ ruber}$ with C 90 isotope record	232	650	1049	38	Lirer et al. (2014)
Graphic correlation $\delta^{18}O_{G.\ ruber}$ with C 90 isotope record	260	337	1300	3	Lirer et al. (2014)
Graphic correlation $\delta^{18}O_{G.\ ruber}$ with C 90 isotope record	299	−421	1613	29	Lirer et al. (2014)
Top acme *Globigerinoides quadrilobatus*	328	−750	2700	48	Lirer et al. (2013)
Base acme *Globigerinoides quadrilobatus*	406	−1750	3700	48	Lirer et al. (2013)
Astroni 3 (tephra layer)	420	−2248	4198	100	Smith et al. (2011)
Agnano M. Spina (tephra layer)	436	−2470	4420	58	Lirer et al. (2013)

to 0.5‰) (Fig. 10) reflects the cold event correlable with the so-called '4.2 ka event' observed at a global scale (from North America, through the Middle East to China; and from Africa, parts of South America, and Antarctica, Mayewski et al., 2004; Staubwasser and Weiss, 2006; Walker et al., 2012).

During the Early Bronze Age, clear evidence of the "4.2 ka" deforestation event is also documented in the pollen record (Fig. 11), where the process of landscape opening, starting at ca. 2700 BCE and reaching a maximum at around 2200 BCE, mostly affected the evergreen vegetation (Fig. 11). Our data are consistent with other pollen records in the

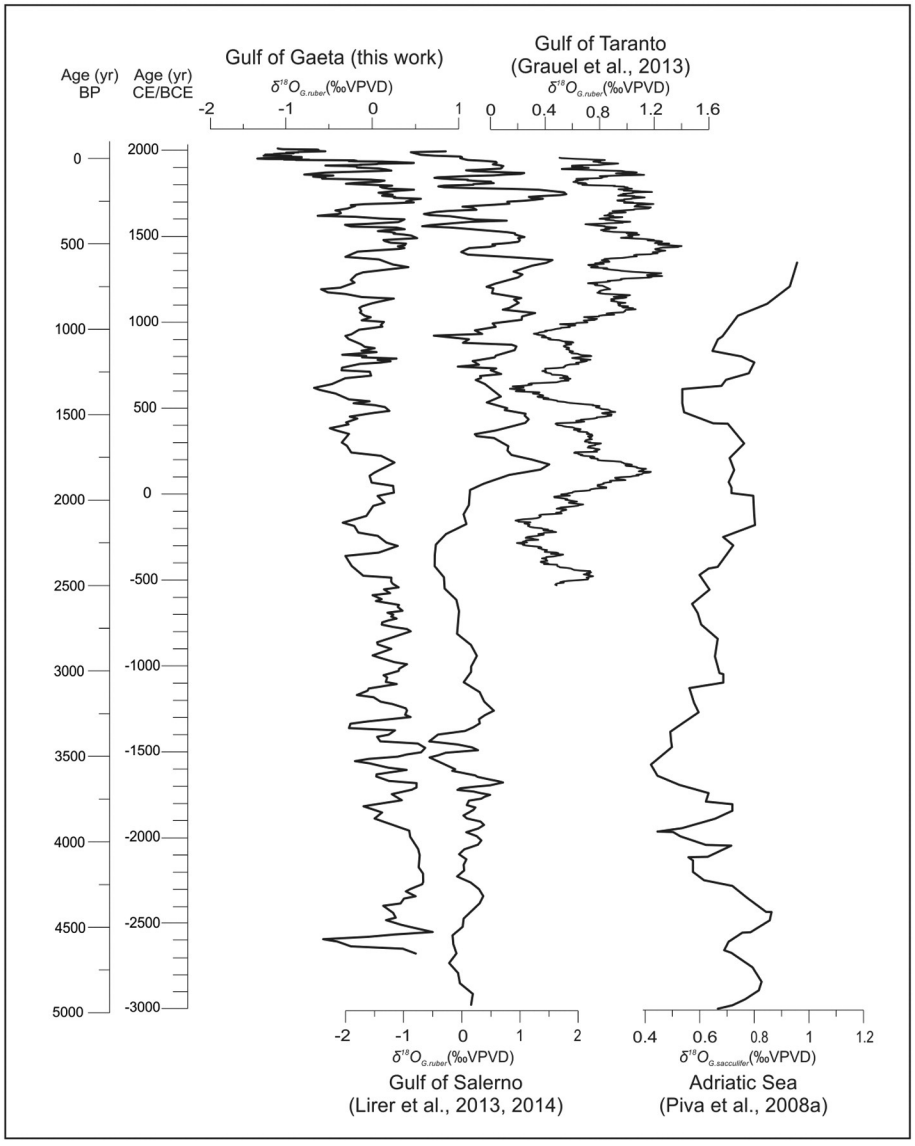

Fig. 8. Comparison in time domain between $\delta^{18}O_{G.\ ruber}$ signals from Gaeta Gulf (this work), Salerno Gulf (Lirer et al., 2013, 2014), Taranto Gulf (Grauel et al., 2013) and $\delta^{18}O_{G.\ sacculifer}$ data from Adriatic Sea (Piva et al., 2008a).

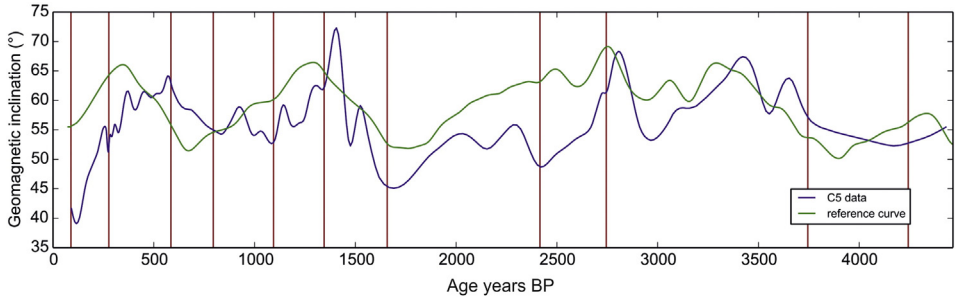

Fig. 9. Measured paleomagnetic inclination curve from core C5, compared with an inclination reference curve calculated from the SHA.DIF.14k geomagnetic model (Pavón-Carrasco et al., 2014) for the site location. The blue line is the measured inclination from the core; the green line is the reference curve; the red bars mark the tie-points which constrain the age model.

Central Mediterranean (south of 43° N), showing a deforestation process (ca. 2500–1900 BCE) that had a great impact on the evergreen forests cover (Sadori and Narcisi, 2001; Di Rita and Magri, 2009; Tinner et al., 2009; Di Rita et al., 2011).

6.1.3. Middle Bronze Age–Iron Age: ca. 1900 BCE to ca. 500 BCE/ca. 3850 BP–ca. 2450 BP

The base of the Middle Bronze Age-Iron Age period at 1900 BCE is marked by a dominance of herbivorous–opportunistic planktonic foraminifera (Fig. 10). This phase is basically characterized by the acme interval (from ca. 1752 BCE to ca. 750 BCE) of planktonic foraminifer *G. quadrilobatus*. This species is indicative of warm, oligotrophic surface waters in summer (Hemleben et al., 1989; Pujol and Vergnaud Grazzini, 1995). Their co-occurrence with *G. ruber* alba and *Orbulina* spp. suggests oligotrophic conditions (at least in summer) during the Middle Bronze Age–Iron Age period. At the same time, the high abundance percentages of the herbivorous–opportunistic species *T. quinqueloba* and *G. glutinata* indicates high productivity surface waters, strong seasonality and the presence of continental runoff. This latter condition is also documented by Zolitschka et al. (2003) in Lake Steisslingen and Lake Holzmaar in Germany, where a period of increasing runoff, between 850 BCE and 750 BCE, was related to wetter climatic conditions (prolonged suppression of radial tree growth).

During the Middle Bronze Age–Iron Age period, we identify two subintervals:

i) from 1850 BCE to 1450 BCE, there is an increase in abundance of warm water taxa *G. quadrilobatus*, *G. siphonifera* and *Orbulina* spp. (Pujol and Vergnaud Grazzini, 1995) associated with *G. elongatus*

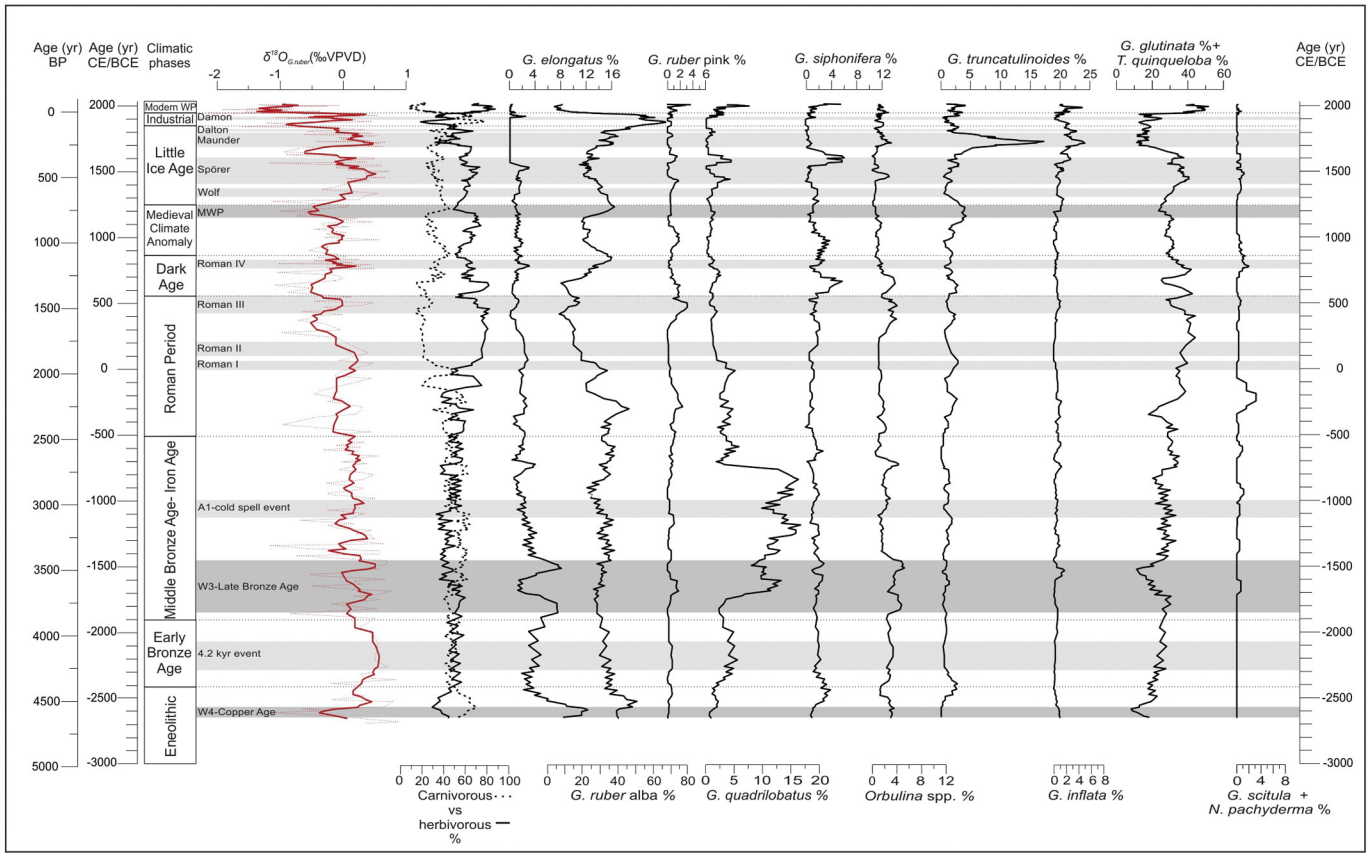

Fig. 10. Comparison in time domain of planktonic foraminifera distribution patterns and $\delta^{18}O_{G.\ ruber}$ data (red dotted line represent the raw data and thick red line is a 5-point moving average) with the position of the climatic phases (Eneolithic, Early Bronze Age, Middle Bronze Age-Iron Age, Roman Period, Dark Age, Medieval Climate Anomaly, Little Ice Age, Industrial Period, Modern Warn Period). We have plotted the distribution pattern of the herbivorous–opportunistic (*T. quinqueloba*, *G. glutinata* and *G. bulloides*) *vs* carnivorous foraminiferal species (*G. ruber* alba variety, *G. quadrilobatus*, *Orbulina* spp. and *G. siphonifera*) to identify the climatic phases. The light grey and dark grey bands indicate the cold and warm phases, respectively.

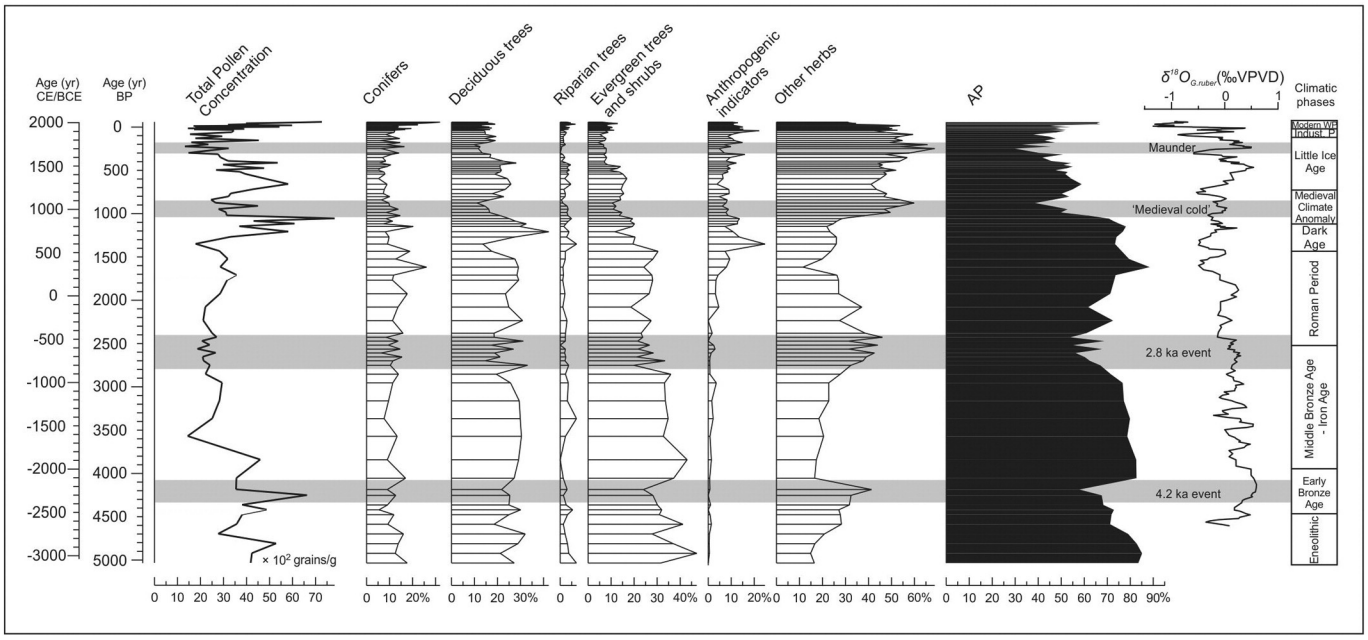

Fig. 11. Pollen diagrams and $\delta^{18}O_{G.ruber}$ data (thick black line represents a 5-point moving average) plotted vs time domain with the position of the identified climatic phases (Eneolithic, Early Bronze Age, Middle Bronze Age–Iron Age, Roman Period, Dark Age, Medieval Climate Anomaly, Little Ice Age, Industrial Period, Modern Warm Period). The grey bands represent the main climatic events detected by pollen data.

increase and lower values of the $\delta^{18}O_{G.\ ruber}$ signal (Fig. 10). We interpret these paleoproxies as the result of a warm phase chronologically correlated with the warm event W3 (Late Bronze Age) reported by Piva et al. (2008a, b) in the Adriatic Sea;

ii) at ca. 1050 BCE, high values in the $\delta^{18}O_{G.\ ruber}$ signal (Fig. 10) result time equivalent to the A1-cold spell event, marked by a decrease in alkenone SST and the C2 cold event (Iron Age) reported in the Adriatic Sea (Sangiorgi et al., 2003; Piva et al., 2008a, b) and in eastern Mediterranean Sea (Rohling et al., 2002).

From 1900 BCE to 900 BCE, pollen data suggest a forested landscape, with a prevalence of evergreen trees and shrubs (Fig. 11). A similar vegetation pattern is observed in many coastal and inland pollen sites of the central Mediterranean region (Di Rita and Magri, 2009, 2012 and references therein), especially those affected by the aridification processes at 4.2 ka BP, where a phase of increased evergreen vegetation (ca. 2000–900 BCE) is clearly recorded after the deforestation. This forest recovery may have been influenced by the establishment of a generally stable humid and warm climate phase, whose regional signature seems reflected also in the pollen record and in the *G. quadrilobatus* acme interval (Fig. 10) of the study core.

Between ca. 900 BCE and 500 BCE a new drop in forest vegetation is recorded, coupled with an increase in *Artemisia* and other xerophytes (Fig. 11). This process may be the effect of new dry climate phase probably induced by the 2.8 ka BP event (Bond event 2) (Bond et al., 2001). This short climate change, was also documented by a decrease in arboreal pollen percentages in the central Mediterranean region (Joannin et al., 2012; Azuara et al., 2015), associated with a decrease in magnetic solar activity (van Geel et al., 2000; Martìn-Puertas et al., 2012).

6.1.4. Roman period: ca. 500 BCE to ca. 550 CE/ca. 2450 BP–ca. 1400 BP

The lowermost part of Roman period is characterized by the occurrence of *G. ruber* pink variety and high abundance of *G. ruber* alba up to ca. 150 BCE (Fig. 10), suggesting warmer climatic conditions with respect to the late Roman Period. This information fits the reconstructed Sea Surface Temperatures in the central-western Mediterranean Sea (Martínez Cortizas et al., 1999; Lirer et al., 2014; Cisneros et al., 2016), documenting consistent marine thermal responses to climatic changes during this time interval.

Between 300 BCE and 100 BCE the abrupt increase of the *G. scitula–N. pachyderma* group (Fig. 10), is interpreted as the result of the winter cold phase between 350 BCE and 100 BCE reported in the historical documents describing frozen Tiber in Rome (Lamb, 1977).

The pollen data in the first 500 years of the Roman period shows relatively open condition, as suggested by appreciable values of herbaceous taxa, including *Artemisia* (Fig. 11).

During the upper part of the Roman Period (at ca. 200 CE), the $\delta^{18}O_{G.\ ruber}$ record shows a change in frequency and amplitude oscillations that corresponds to an increase in abundance (up to 80%) of herbivorous–opportunistic planktonic foraminifera (Fig. 10). This $\delta^{18}O_{G.\ ruber}$ signature allows to identify three cold intervals, previously documented by Lirer et al. (2014), which can be correlated with the solar activity (Roman I, Roman II and Roman III) (Fig. 10). These phases are characterized by a slightly decrease in abundance of high surface water planktonic foraminiferal indicators *T. quinqueloba* and *G. glutinata*, probably associated to the low temperatures and absence of runoff. Moreover, the observed distributional pattern of *G. ruber* pink variety, the occurrence of *G. scitula–N. pachyderma* group and the strong decrease in abundance of *T. quinqueloba* - *G. glutinata* group (Fig. 10) suggests relatively wetter conditions during summer and cold-dry ones during winter only during the Roman III event. Between 100 and 450 CE, the pollen record shows a marked expansion of the forest cover (AP ca. 90%, peaking around 350 CE), suggesting humid climate conditions.

6.1.5. Dark Age: ca. 550 to ca. 860 CE/ca. 1400 BP–ca. 1090 BP

The early Dark Age (from 550 to 750 CE) is characterized by warm climatic conditions documented by $\delta^{18}O_{G.\ ruber}$ values (−0.5‰) and the increase of warm water species *G. ruber*, *G. siphonifera* and *Orbulina* spp. (Fig. 10). These species are currently very abundant in the Tyrrhenian Sea, especially in the Gulf of Naples (De Castro Coppa et al., 1980; Pujol and Vergnaud Grazzini, 1995; Sprovieri et al., 2003).

In the upper part of this interval (from 750 to 860 CE), the $\delta^{18}O_{G.\ ruber}$ signal associated with maximum abundance of the cold *G. scitula–N. pachyderma* group and a decrease in warm water species, shows a cooling event corresponding to the Roman IV Period (Fig. 10). This event, documented also in the Salerno Gulf (southern Tyrrhenian Sea) by Lirer et al. (2014), agrees with the $\delta^{18}O$ records of the Taranto Gulf (Grauel et al., 2013) and Adriatic Sea (Piva et al., 2008a,b) (Fig. 8), but

shows some differences with the western Mediterranean Sea (Cisneros et al., 2016), probably due to the different resolution scale.

Between 50 and 650 CE, a decline in the values of trees suggests a reduction of forest cover (Fig. 11). This was facilitated by a rapid decrease in both evergreen and deciduous broadleaved taxa, as well in conifers, although a marked expansion of *Castanea*, among anthropogenic indicators, contributed to keep high the tree percentage values. This complex forest dynamics may be explained by the influence of cooler climate and decreased humidity (cf. Dark Ages Cold Period), which may have had a significant impact on the development of the natural tree populations, already cleared by man in favour of chestnut forestry.

The dryness, characterizing the Dark Age, is correlable with decreased humidity in the western Mediterranean (Nieto-Moreno et al., 2011), evidenced by forest cover regression episodes (Jalut et al., 2000, 2009; Combourieu-Nebout et al., 2009), a decrease in river activity in southern Europe (Magny et al., 2002; Macklin et al., 2006), cooling events in the Balearic Basin (Frigola et al., 2007) and lower lake levels in southern Spain (Carrión, 2002).

6.1.6. Medieval Climate Anomaly (MCA): ca. 860 to ca. 1250 CE/ca. 1090 BP–ca. 700 BP

The transition between the Dark Age and the Medieval Climate Anomaly (MCA) Period is associated to the transition from carnivorous to herbivorous–opportunistic planktonic species that culminate at 1220 CE, when the carnivorous taxa dominate (Fig. 10).

Several authors (e.g., Lamb, 1977; Jones et al., 2004; Mann et al., 2009; Büntgen and Tegel, 2011) described this interval as a relatively stable and warm period. The planktonic foraminifera from this time interval document a general temperate climate condition as testified by the coexistence of warm and cold species in the planktonic foraminiferal assemblage (Fig. 10). In addition, a reduction in abundance of *G. ruber* alba from ca. 1000 to ca. 1100 CE associated with a slight increase of *G. ruber* pink, seems to suggest less temperate and humid conditions. During this short time interval, the decrease in deciduous trees and a considerable parallel increase in herbaceous taxa document a rapid and significant opening of the vegetation landscape. This expansion of herbaceous communities may have been favoured by an oscillation towards a more arid and cool climate. (Fig. 11).

Similar dry conditions are also documented in the Iberian Peninsula (Moreno et al., 2012) based on multiproxy evidence (e.g. lake levels decrease, presence of xerophytic and heliophytic vegetation, low frequency of floods, major Saharan eolian fluxes, and less fluvial input to marine basins) and in the Alboran Sea basin (Nieto-Moreno et al., 2013).

Between 1220 and 1250 CE, a marked shift in $\delta^{18}O_{G.\ ruber}$ signal towards negative values, associated with a strong increase in *G. ruber* abundance, document the warmest interval (Medieval Warm Period) occurring during the MCA (Fig. 10). At that time, the increase in abundance of *G. truncatulinoides* (Fig. 10) suggests the presence of a deep mixed layer during winter.

During this short time interval, pollen data show a new forest recovery, mostly related to an increase in both deciduous and evergreen arboreal taxa, suggesting a climate change towards more warm and humid condition that favoured the growth of broadleaved populations (Fig. 11).

This climate feature may be correlated with the abrupt increase of ~1–1.5 °C in the SST profile occurring around 980 CE in the North Icelandic (Sicre et al., 2008).

6.1.7. Little Ice Age period (LIA): ca. 1250 to 1850 CE/ca. 700 BP–ca. 100 BP

The MCA–LIA transition is the last global-scale Rapid Climatic Change (RCC) event reported in the Holocene by Mayewski et al. (2004) and is recognizable also in the Mediterranean marine records (e.g., Piva et al., 2008a,b; Incarbona et al., 2010; Lirer et al., 2014; Goudeau et al., 2015). This transition is marked by an important change in nutrient availability in water column (Lirer et al., 2014), documented by the change from carnivorous to herbivorous–opportunistic planktonic foraminifera taxa (Fig. 10). The high-resolution $\delta^{18}O_{G.ruber}$ data allowed us to identify, within the Little Ice Age, four climatic oscillations related to solar activity: Wolf, Spörer, Maunder and Dalton cold events (Fig. 10), also already documented in the Gulf of Salerno (Lirer et al., 2014).

The Wolf and Spörer climatic phases are characterized by a shift to cooler conditions suggested by the increase of cool water planktonic foraminiferal species *G. inflata*, *G. truncatulinoides* and *G. scitula - N. pachyderma* group, by a decrease of the warm water taxon *G. ruber* (Fig. 10) and by an increase of high productivity surface waters taxa (*G. glutinata - T. quinqueloba*) (Fig. 10). The increase in regime productivity agrees with the results obtained in the Sicily Channel and in the Adriatic Sea (Piva et al., 2008a,b; Incarbona et al., 2010; Siani et al., 2013) and in the western Mediterranean Basin (Nieto-Moreno et al., 2011). This might indicate a larger southward extension of the westerlies leading to increase in precipitation and thus an enhanced outflow of the rivers during this interval.

Around 1600 CE a shift of $\delta^{18}O_{G.\ ruber}$ signal from 0.5‰ to −1‰ and the increase of warm-water taxa *G. siphonifera* and *G. quadrilobatus* marked the warm interval between Spörer and Maunder (Fig. 10).

The onset of the Maunder is characterized by a strong increase of abundance of *G. truncatulinoides* and *G. inflata* (Fig. 10) suggesting the presence of a deep mixed layer during winter. This oceanographic feature can be induced by the increase in winds intensity probably due to Atmospheric blocking events. Atmospheric blocking events are mid-latitude weather systems where a quasi-stationary high-pressure system, located in the Northeast Atlantic, modifies the flow of the westerly winds by blocking or diverting their pathway (Moffa Sánchez et al., 2014).

Blocking is accompanied by cold winter temperatures in Western Europe; the climatological maximum in winter blocking days is located over Western Europe, with a secondary maximum over Greenland (Häkkinen et al., 2011). Variability of atmospheric blocking over years to several decades shows correlation with the ocean surface temperature and with significant changes in Atlantic Ocean circulation, mediated by wind-stress curl and air-sea heat exchange (Häkkinen et al., 2011).

The Maunder Minimum (MM) represents the coldest period of the Little Ice Age, an interval of reduced solar activity. Within the MM, the Late Maunder Minimum was a period of persistent extremely cold winters in Europe (Barriopedro et al., 2008). Barriopedro et al. (2008) relate the particular cooling recorded in Maunder in the Northern Hemisphere to events of Atlantic blocking. Moffa Sánchez et al. (2014) shows that small-scale atmospheric patterns in the North-East Atlantic, such as atmospheric blocking events as part of the east Atlantic pattern or polar mesoscale storms, may considerably contribute to driving North Atlantic surface circulation.

At the end of the LIA, around in 1850 CE, a strong change in the pattern of carnivorous and herbivorous planktonic foraminifera is recorded (Fig. 10).

The pollen record shows a new significant decrease in forest cover (Fig. 11). This process started at ca. 1300 CE and ended ca. 1850 CE, in good agreement with the chronological evidence of the LIA interval. The deforestation process seems to have particularly affected the broadleaved taxa, whose curves show the lowest percentage values of the entire sequence between 1650 and 1750 CE, in correspondence with the Maunder Minimum (Fig. 11). The cool climate associated with this minimum of solar activity may have affected the development of many arboreal taxa populations, except conifers that show a moderate increase (Fig. 11).

6.1.8. Industrial period: ca. 1850–1950 CE

The Industrial Period is characterized by an increase of warm water species *G. quadrilobatus* and *G. ruber* that reached here their maximum

percentages (Fig. 10). The coexistence of these taxa indicates the presence of the mixed layer in the water column (Spooner et al., 2005).

The onset of Damon (approximately 1900 CE) is marked by a *G. ruber* pink and *G. elongatus* peak suggesting a warm conditions confirmed by the absence of cold planktonic foraminiferal taxa *G. truncatulinoides* and *G. inflata* (Fig. 10). This record is consistent with studies performed in the Gulf of Taranto that report an increase in temperature at the beginning of the 20th century (Taricco et al., 2009; Grauel et al., 2013).

The dominance of herbivorous–opportunistic planktonic foraminiferal species and the $\delta^{18}O_{G.\ ruber}$ signature can be interpreted as the occurrence of a humid climatic phase during the entire Industrial Period from approximately 1850 CE to 1940 CE as reported by Nieto-Moreno (2012) in the western Mediterranean region. A clear trend towards humid conditions is also clearly reflected by the pollen record, which highlights a general arboreal forest development, mostly due to conifers and evergreen broadleaved populations (Fig. 11).

6.1.9. Modern Warm Period: 1950 CE to the present day

The onset of the Modern Warm Period is characterized by a strong increase in *G. glutinata* and *T. quinqueloba* abundances suggesting high surface productivity (Fig. 10). At same time, *G. ruber* alba shows an abrupt decrease in abundance and $\delta^{18}O_{G.ruber}$ signal records the most prominent negative excursion (Fig. 10) of the last two millennia (from 0.5‰ to −1.5‰). These features have been previously documented by Lirer et al. (2014) in the Salerno Gulf (south Tyrrhenian Sea), suggesting a possible human overprint on global warm climate condition during the last 50 years. During this period, Vallefuoco et al. (2012) documented, in the marine record of Gulf of Salerno (south Tyrrhenian Sea), also a rapid increase of benthic foraminifer *Bulimina aculeata*, suggesting high productivity conditions (Corliss, 1985; Mackensen and Douglas, 1989; Jorissen et al., 1992; Sen Gupta and Machain-Castillo, 1993; Rathburn and Corliss, 1994). We speculate that these micropaleontological features, with an increase in organic matter flux associated to strong increase in planktonic foraminifera related to high-surface water productivity and coexistence of oligotrophic condition [abundance increase of *G. quadrilobatus* in the study core and in the Gulf of Salerno (Lirer et al., 2014)], could confirm a strong overprint from human activities. During this interval in fact the building of dams in central-southern Tyrrhenian coastal zones during the middle of last century resulted in a strong reduction of coarse- grained materials, which caused a change in sediment size and a possible change in nutrient supply, as hypothesized by Vallefuoco et al. (2012). The human impact on natural ecosystems is also visible in the arboreal vegetation which is dominated by *Pinus* and reflects extensive plantation of pine forests in the coastal areas of the Gulf of Gaeta (Fig. 11). In addition, the nearby territory was increasingly occupied by cultivations of *Olea*, *Vitis*, cereals and hemp, confirming intensive land exploitation for agriculture (Fig. 11).

6.2. North Atlantic Oscillations (NAO) index vs marine multiproxy in the central Mediterranean Sea

Atmospheric circulation patterns in the northern hemisphere influence climate variability in the Mediterranean region (Jalut et al., 1997, 2000; Combourieu Nebout et al., 2002; Goy et al., 2003; Roberts et al., 2012; Fletcher et al., 2012). The NAO is the most important mode of variability in the atmospheric circulation over the North Atlantic, with considerable influences winter temperature/precipitation throughout the Eurasian continent and eastern North America (Greatbatch, 2000). However, the interpretation of the NAO effect in the Mediterranean area is ambiguous because the NAO influence is not stationary through time and space and also because it is a dominant mode only in winter (e.g., Xoplaki et al., 2008). In general, there is a high-pressure system over the subtropical region near the Azores, and a low-pressure situation over the subpolar region near Iceland (Wanner et al., 2001). Within this configuration, the NAO index gets positive in a stronger phase with a high-pressure gradient and negative in phases with a weaker pressure gradient (Brönnimann, 2005). In Italy, the NAO index modulates the winter precipitation (Brunetti et al., 2002; Tomozeiu et al., 2002; Caloiero et al., 2011; López-Moreno et al., 2011; Casanueva et al., 2014; Benito et al., 2015) following a opposite trend with respect to the northern Europe (López-Moreno et al., 2011; Benito et al., 2015; and references therein). The NAO forcing has been shown also in the fossil marine sedimentary archives (i.e., Chen et al., 2011; Nieto-Moreno et al., 2013; Goudeau et al., 2015; Jalali et al., 2015) and consequently may be important to document this forcing also in the high-resolution shallow-water marine record of the central Tyrrhenian Sea.

The comparison between NAO index (Trouet et al., 2009; Olsen et al., 2012), $\delta^{18}O_{G.ruber}$ signal, planktonic foraminiferal herbivorous *versus* carnivorous taxa and pollen AP index shows important features useful to understand global forcing within this central area of the Mediterranean region (Fig. 12).

The positive NAO index from 2500 BCE to about 900 BCE is not interrupted by significant polarity change, in contrast from 900 to 100 BCE is characterized by a generally negative NAO index. The long term comparison between the NAO index and the $\delta^{18}O_{G.\ ruber}$ signal shows an overall antithetic correlation (even though peak-to-peak correlation is not possible due to the different resolution of the two proxies) during the last five millennia, with the exception of scattered parallelism between 0 and 200 CE, probably due to the local overprint (Fig. 12). This antithetic trend supports the NAO reconstruction of López-Moreno et al. (2011): when the NAO index is positive south Europe climate is mild and dry; on the contrary, a negative index is associated with the reverse pattern.

Following the cooling phase related to the cold 2.8 ka event (Bond cycle 2), from beginning of the Roman Period (ca.500 BCE) upwards, the climate system displays a turnover *vs* a more positive NAO index associated with a long-term trend to lower $\delta^{18}O_{G.\ ruber}$ values and with a significant planktonic foraminiferal changes from carnivorous *vs* herbivorous–opportunistic species (Fig. 12). The herbivorous–opportunistic species are the dominant group over most of the last two millennia suggesting a strong connection with nutrient availability. In addition, from Dark Age (ca. 500 CE) upwards, the Mediterranean planktonic foraminiferal $\delta^{18}O$ data (Fig. 8) document a synchronous progressive long-term shift to more positive values (cooling trend) as recently documented by Cisneros et al. (2016) from SST stack of the Menorca basin.

This climate mode seems to change again around 1450 CE (mid Little Ice Age) when the NAO index starts to change to negative values and the $\delta^{18}O_{G.\ ruber}$ record shifts towards higher values (Fig. 12), suggesting the onset of the modern warm climate condition.

Pollen data, suggesting stable warm climate conditions between 1900 and 900 BCE, seem to be in agreement with the aforementioned NAO index reconstruction by López-Moreno et al. (2011). In the last two millennia, distinguishing the influence of climate from human activity in pollen records is a very challenging task. However, some pronounced vegetation fluctuations, also reflected in the NAO index record, may be interpreted as mainly influenced by climate changes. In particular, during the Maunder minimum of the Little Ice Age, a phase of negative NAO, associated with cool climate, may have caused a major decrease of broadleaved forest cover, due both to its direct influence on tree growth and to increased human pressure on woodlands for firewood provision. A strong climate influence on vegetation may be also envisaged during the Medieval Climate Anomaly, when a rapid oscillation of the NAO index corresponds to a clear decrease in the arboreal vegetation (Fig. 12). When the NAO index reached its minimum, between 1000 and 1100 CE, the forest cover may have suffered a cooling of climate. Conversely, when the NAO index started to increase after 1100 CE, population of trees expanded, probably in response to the establishment of milder conditions (Fig. 12).

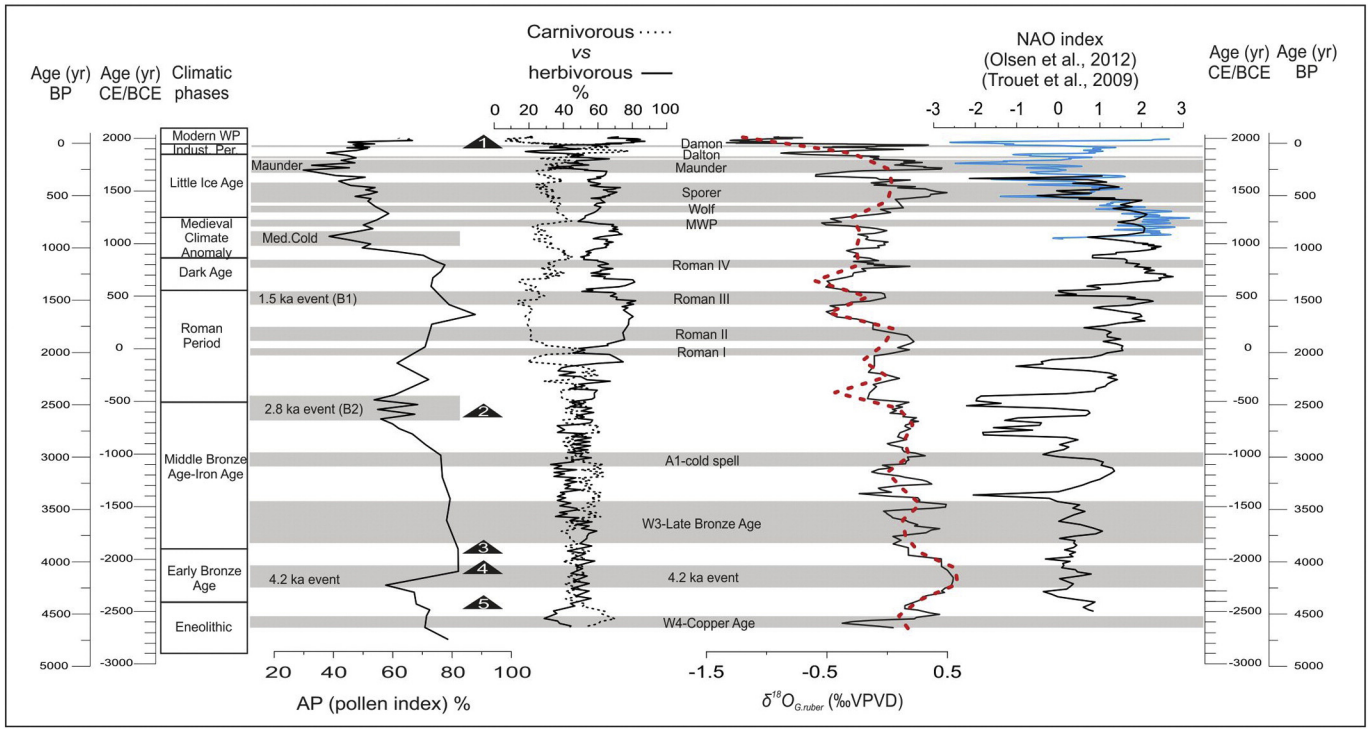

Fig. 12. Comparison in time domain between the AP pollen data index, planktonic foraminiferal turnover (carnivorous vs herbivorous–opportunistic species), $\delta^{18}O_{G.\ ruber}$ signal (5 point moving average black line and 150 years moving average thick red dotted line) and NAO index (black line by Olsen et al., 2012; blue line by Trouet et al., 2009). The grey bands represent the identified climatic events. The labels 2.8 ka event (B2) and 1.5 ka event (*B1*) correspond to the position of Bond events 1 and 2 (Bond et al., 2001). The label Med. cold corresponds to Medieval cold. Modern WP = Modern Warm Period; Indust. Per. = Industrial Period. The black triangles with the number from 1 to 5 are the position of the identified tephra layers: 1—Vesuvius (1906 CE), 2—Vateliero–Ischia (2.4–2.6 ka BP), 3—Capo Miseno (3.9 ka BP), 4—Astroni3 (4.1–4.3 ka BP), 5—Agnano M. Spina (4.42 ka BP).

7. Conclusions

In this study, we used a multi-proxy approach in order to investigate the paleoclimate variability in the central Mediterranean region during the late Holocene. The robust chronological control performed on radionuclides, tephrostratigraphy and isotopic stratigraphy allows a reconstruction at a century scales since 2900 BCE. Nine main intervals have been identified and correlated with the archaeological/cultural periods: Eneolithic (base of the core–ca. 2410 BCE), Early Bronze Age (ca. 2410 BCE–ca. 1900 BCE), Middle Bronze Age–Iron Age (ca. 1900 BCE–ca. 500 BCE), Roman Period (ca. 500 BCE–ca. 550 CE), Dark Age (ca. 550 CE–ca. 860 CE), Medieval Climate Anomaly (ca. 860 CE–ca. 1250 CE), Little Ice Age (ca. 1250 CE–ca. 1850 CE), Industrial Period (ca. 1850 CE–ca. 1950 CE), Modern Warm Period (ca. 1950 CE–present day). Within these time intervals, our multiproxy record shows several short-term climate oscillations, adding new details to the records studied in different areas of the Mediterranean Basin (Alboran Sea, Gulf of Salerno, Gulf of Taranto, Adriatic Sea and Ionian Sea). A strong modification in climate system occurs from the onset of the Roman Period up to the present-day, recorded by long term trend and amplitude oscillations of the $\delta^{18}O_{G.\ ruber}$ signal, by the onset of main planktonic foraminiferal turnover from carnivorous to herbivorous–opportunistic species, and by the consistent fluctuations of the pollen records.

The good correspondence between the observed climate oscillations and recognized archaeological intervals underline the role exerted by climate change in determining rises and declines of civilizations.

In addition, the antithetic correlation between the NAO index and $\delta^{18}O_{G.\ ruber}$ signal suggests a global climate signature in the shallow water marine study record, and in particular, when the NAO index is positive south Europe climate is mild and dry; on the contrary, a negative index is associated with the reverse pattern, suggesting a hemispheric-scale atmospheric connection.

Supplementary data to this article can be found online at http://dx.doi.org/10.1016/j.gloplacha.2016.04.007.

Acknowledgments

The cores SW-104-C5 and C5 have been collected by IAMC-CNR (Napoli) aboard of the CNR-Urania vessel during the oceanographic cruise I-AMICA-2013. Many thanks are given to the Editor and the two anonymous reviewers for their constructive comments for improving the manuscript. This research has been financially supported by the Project of Strategic Interest NextData PNR 2011–2013 (www.nextdataproject.it) and RITMARE (PNR 2012-2016) project (www.ritmare.it). This is ISMAR-CNR contribution number 1882.

References

Amato, V., Aucelli, P.P.C., D'Argenio, B., Da Prato, S., Ferraro, L., Pappone, G., Petrosino, P., Rosskopf, C.M., Russo Ermolli, E., 2012. Holocene environmental evolution of the coastal sector in front of the Poseidonia–Paestum archaeological area (Sele plain, southern Italy). Rendiconti Lincei-Scienze Fisiche e Naturali 23, 45–59.

Artale, V., Astraldi, M., Buffoni, G., Gasparini, G.P., 1994. Seasonal variability of gyre-scale circulation in the northern Tyrrhenian Sea. J. Geophys. Res. 99 (C7), 14127–14137.

Astraldi, M., Gasparini, G.P., 1994. The seasonal characteristics of the circulation in the Tyrrhenian Sea. In: La Violette, P. (Ed.), Seasonal and Interannual Variability of the Western Mediterranean SeaCoastal and Estuarine Studies Vol. 46. American Geophysical Union, Washington, D.C., pp. 115–134.

Azuara, J., Combourieu-Nebout, N., Lebreton, V., Mazier, F., Müller, S.D., Dezileau, L., 2015. Late Holocene vegetation changes in relation with climate fluctuations and human activities in Languedoc (Southern France). Clim. Past 11, 1769–1784.

Bàrcena, M.A., Flores, J.A., Sierro, F.J., Pérez-Folgado, M., Fabres, J., Calafat, A., Canals, M., 2004. Planktonic response to main oceanographic changes in the Alboran Sea (Western Mediterranean) as documented in sediment traps and surface sediments. Mar. Micropaleontol. 53, 423–445.

Barriopedro, D., Garcìa-Herrera, R., Huth, R., 2008. Solar modulation of Northern Hemisphere winter blocking. J. Geophys. Res. 113, D14118.

Barsotti, S., Neri, A., Bertagnini, A., Cioni, R., Mulas, M., Mundula, F., 2015. Dynamics and tephra dispersal of violent Strombolian eruptions at Vesuvius: insights from field data, wind reconstruction and numerical simulation of the 1906 event. Bull. Volcanol. 77, 58. http://dx.doi.org/10.1007/s00445-015-0939-6.

Bé, A.W.H., 1977. An ecologic, zoogeographic and taxonomic review of recent planktonic foraminifera. Oceanic Micropaleontology 1, 1–100. Academic Press, London.

Bé, A.W.H., Hutson, W.H., 1977. Ecology of Planktonic Foraminifera and Biogeographic Patterns of Life and Fossil Assemblages in the Indian Oceanic Micropaleontology 23. Academic Press, London, pp. 369–414.

Bé, A.W.H., Tolderlund, D.S., 1971. Distribution and ecology of living foraminifera in surface waters of the atlantic and indian oceans. In: Funnel, B.M., Riedel, W.R. (Eds.), The Micropaleontology of the Oceans. Cambridge University Press, London (105–4).

Bellucci, L.G., Frignani, M., Cochran, J.K., Albertazzi, S., Zaggia, L., Cecconi, G., 2007. ^{210}Pb and ^{137}Cs as chronometers for salt marsh accretion in the Venice Lagoon — links to flooding frequency and climate change. J. Environ. Radioact. 97, 85–102.

Benito, G., Macklinb, M.G., Zielhofer, C., Jones, A.F., Machado M.J., 2015. Holocene flooding and climate change in the Mediterranean. Catena 130, 13–33.

Bergamasco, A., Malanotte-Rizzoli, P., 2010. The circulation of the Mediterranean Sea: a historical review of experimental investigations. Adv. Oceanogr. Limnol. 1, 11–28.

Beug, H.J., 2004. Leitfaden der Pollenbestimmung fur Mitteleuropa und angrenzende Gebiete. Verlag Friedrich Pfeil, Munich.

Blasi, C., Capotorti, G., Copiz, R., Guida, D., Mollo, B., Smiraglia, D., Zavattero, L., 2014. Classification and mapping of the ecoregions of Italy. Plant. Biosyst. 148, 1255–1345.

Bond, G., Kromer, B., Beer, J., Muscheler, R., Evans, M.N., Showers, W., Hoffmann, S., Lotti-Bond, R., Hajdas, I., Bonani, G., 2001. Persistent solar influence on North Atlantic climate during the Holocene. Science 294, 2130.

Bonomo, S., Cascella, A., Alberico, I., Ferraro, L., Giordano, L., Lirer, F., Vallefuoco, M., Marsella, E., 2014. Coccolithophores from near the Volturno estuary (central Tyrrhenian Sea). Mar. Micropaleontol. 111, 26–37.

Brönnimann, S., 2005. Grossräumige Klimaschwankungen. Skript zur Vorlesung (www.iac.ethz.ch.).

Brunetti, M., Maugeri, M., Nanni, T., 2002. Atmospheric circulation and precipitation in Italy for the last 50 years. Int. J. Climatol. 22, 1455–1471.

Budillon, F., Esposito, E., Iorio, M., Pelosi, N., Porfido, S., Violante, C., 2005. The geological record of storm events over the last 1000 years in the Salerno Bay (Southern Tyrrhenian Sea): new proxy evidences. Adv. Geosci. 2, 123–130.

Budillon, F., Lirer, F., Iorio, M., Macri, P., Sagnotti, L., Vallefuoco, M., Ferraro, L., Garziglia, S., Innangi, S., Sahabi, M., Tonielli, R., 2009. Integrated stratigraphic reconstruction for the last 80 kyr in a deep sector of the Sardinia Channel (Western Mediterranean). Deep Sea Res., Part II 56, 725–737.

Büntgen, U., Tegel, W., 2011. European tree-ring data and the Medieval Climate Anomaly. PAGES 19, 14–15.

Büntgen, U., Myglan, V.S., Ljungqvist, F.C., McCormick, M., Di Cosmo, N., Sigl, M., Jungclaus, J., Wagner, S., Krusic, P.J., Esper, J., Kaplan, J.O., de Vaan, M.A.C., Luterbacher, J., Wacker, L., Tegel, W., Kirdyanov, A.V., 2016. Cooling and societal change during the Late Antique Little Ice Age from 536 to around 660 AD. Nat. Geosci.

Caloiero, T., Coscarelli, R., Ferrari, E., Mancini, M., 2011. Precipitation change in Southern Italy linked to global scale oscillation indexes. Nat. Hazards Earth Syst. Sci. 11, 1683–1694.

Capotondi, L., Principato, M.S., Morigi, C., Sangiorgi, F., Maffioli, P., Giunta, S., Negri, A., Corselli, C., 2006. Foraminiferal variations and stratigraphic implications to the deposition of sapropel S5 in the eastern Mediterranean. Palaeogeogr. Palaeoclimatol. Palaeoecol. 235, 48–65.

Capotondi, L., Girone, A., Lirer, F., Bergami, C., Verducci, M., Vallefuoco, M., Afferri, A., Ferraro, L., Pelosi, N., De Lange, G.J., 2016. Central Mediterranean Mid-Pleistocene paleoclimatic variability and its association with global climate. Palaeogeogr. Palaeoclimatol. Palaeoecol. 442, 72–83.

Carrión, J.S., 2002. Patterns and processes of Late Quaternary environmental change in a montane region of southwestern Europe. Quat. Sci. Rev. 21, 2047–2066.

Casanueva, A., Rodríguez-Puebla, C., Frías, M.D., González-Reviriego, N., 2014. Variability of extreme precipitation over Europe and its relationships with teleconnection patterns. Hydrol. Earth Syst. Sci. 18, 709–725.

Casford, J.S.L., Rohling, E.J., Abu-Zied, R.H., Cooke, S., Fontanier, C., Leng, M.J., Lykousis, V., 2002. Circulation changes and nutrient concentrations in the late Quaternary Aegean Sea: a nonsteady state concept for sapropel formation. Paleoceanography 17 (2). http://dx.doi.org/10.1029/2000PA000601 (doi: 1024).

Catalano, I., Mingo, A., Migliozzi, A., Sgambato, S., Aprile, G.G., 2010. Wood macrolichen *lobaria pulmonaria* on chestnut tree crops: the case study of Roccamonfina Park (Campania region—Italy). Proceedings of the IUFRO Landscape Ecology Working Group International Conference, pp. 188–193.

Chen, L.L., Johannessen, O.M., Wang, H.J., Ohmura, A., 2011. Accumulation over the Greenland ice sheet as represented in reanalysis data. Adv. Atmos. Sci. 28, 1030–1038.

Cisneros, M., Cacho, I., Frigola, J., Canals, J.M., Masqué, P., Martrat, B., Casado, M., Grimalt, J.O., Pena, L.D., Margaritelli, G., Lirer, F., 2016. Sea surface temperature variability in the central-western Mediterranean Sea during the last 2700 years: a multi-proxy and multi-record approach. Clim. Past 12, 849–869.

Cita, M.B., Vergnaud Grazzini, C., Robert, C., Chamley, H., Ciaranfi, N., D'Onofrio, S., 1977. Paleoclimatic record of a long deep sea core from the eastern Mediterranean. Quat. Res. 8, 205–235.

Combourieu Nebout, N., Turon, J., Zahn, R., Capotondi, L., Londeix, L., Pahnke, K., 2002. Enhanced aridity and atmospheric high-pressure stability over the western Mediterranean during the North Atlantic cold events of the past 50 ky. Geology 30 (10), 863–866.

Combourieu-Nebout, N., Peyron, O., Dormoy, I., Desprat, S., Beaudouin, C., Kotthoff, U., Marret, F., 2009. Rapid climatic variability in the West Mediterranean during the last 25,000 years from high resolution pollen data. Clim. Past 5, 503–521.

Corliss, B.H., 1985. Microhabitats of benthonic foraminifera within Mediterranean Sea during times of sapropel S5 and S6 deposition. Palaeogeogr. Palaeoclimatol. Palaeoecol. 190, 139–164.

Corselli, C., Principato, M.S., Maffioli, P., Crudeli, D., 2002. Changes in planktonic assemblages during sapropel S5 deposition: evidence from Urania Basin area, eastern Mediterranean. Paleoceanography 17, 1–30.

Corte-Real, J., Zhang, X., Wang, X., 1995. Large-scale circulation regimes and surface climatic anomalies over the Mediterranean. Int. J. Climatol. 15, 1135–1150.

Croce, A., Nazzaro, R., 2012. The orchid flora of Roccamonfina-Foce Garigliano Regional Park (Campania, Italy). J. Europäischer Orchideen 44, 509–583.

D'Antonio, M., Tonarini, S., Arienzo, I., Civetta, L., Dallai, L., Moretti, R., Orsi, G., Andria, M., Trecalli, A., 2013. Mantle and crustal processes in the magmatism of the Campania region: inferences from mineralogy, geochemistry, and Sr–Nd–O isotopes of young hybrid volcanics of the Ischia island (South Italy). Contrib. Mineral. Petrol. 165, 1173–1194.

de Alteriis, G., Fedi, M., Passaro, P., Siniscalchi, A., 2006. Magneto-seismic interpretation of subsurface volcanism in the Gaeta Gulf (Italy, Tyrrhenian Sea). Ann. Geophys. 49, 4/5.

De Castro Coppa, M.G., Moncharmont Zei, M., Placella, B., Sgarrella, F., Taddei Ruggiero, E., 1980. Distribuzione stagionale e verticale dei Foraminiferi planctonici del Golfo di Napoli. Boll. Soc. Nat. Napoli 89, 1–25.

De Pippo, T., Donadio, C., Pennetta, M., 2003–2004. Morphological control on sediment dispersal along the southern Tyrrhenian coastal zones (Italy). Geol. Romana 37, 113–121.

de Vita, S., Orsi, G., Civetta, L., Carandente, A., D'Antonio, M., Di Cesare, T., Di Vito, M., Fisher, R.V., Isaia, R., Marotta, E., Ort, M., Pappalardo, L., Piochi, M., Southon, J., 1999. The Agnano–Monte Spina eruption (4.1 ka) in the resurgent, nested Campi Flegrei caldera (Italy). J. Volcanol. Geotherm. Res. 91, 269–301.

de Vita, A., Sansivero, F., Orsi, G., Marotta, E., Piochi, M., 2010. Volcanological and structural evolution of the Ischia resurgent caldera (Italy) over the last 10 ky. Geological Society of America Special Issue 464, 193–239.

Di Bella, L., Frezza, V., Bergamin, L., Carboni, M.G., Falese, F., Martorelli, E., Tarragoni, C., Chiocci, F.L., 2014. Foraminiferal record and high resolution seismic stratigraphy of the Late Holocene succession of the submerged Ombrone River delta (Northern Tyrrenian Sea, Italy). Quat. Int. 328-329, 287–300.

Di Pietro, R., 2011. New dry grassland associations from the Ausoni–Aurunci mountains (Central Italy) — syntaxonomical updating and discussion on the higher rank syntaxa. Hacquetia 10, 183–231.

Di Renzo, V., Arienzo, I., Civetta, L., D'Antonio, M., Tonarini, S., Di Vito, M.A., Orsi, G., 2011. The magmatic feeding system of the Campi Flegrei caldera: architecture and temporal evolution. Chem. Geol. 281, 227–241.

Di Rita, F., Magri, D., 2009. Holocene drought, deforestation, and evergreen vegetation development in the central Mediterranean: a 5,500 year record from Lago Alimini Piccolo, Apulia, southeast Italy. The Holocene 19, 295–306.

Di Rita, F., Magri, D., 2012. An overview of the Holocene vegetation history from the central Mediterranean coasts. J. Mediterr. Earth Sci. 4, 35–52.

Di Rita, F., Simone, O., Caldara, M., Gehrels, W.R., Magri, D., 2011. Holocene environmental changes in the coastal Tavoliere Plain (Apulia, southern Italy): a multiproxy approach. Palaeogeogr. Palaeoclimatol. Palaeoecol. 310, 139–151.

Fægri, K., Kaland, P.E., Krzywinski, K., 1989. In: Iversen, IV (Ed.), Textbook of Pollen Analysis by Knut Fægri and Johs. John Wiley & Sons, Chichester.

Fairbanks, R.G., Wiebe, P.H., 1980. Foraminifera and chlorophyll maximum: vertical distribution, seasonal succession, and paleoceanographic significance. Science 209, 1524–1526.

Fletcher, W.J., Debret, M., Sanchez Goñi, M., 2012. Mid-Holocene emergence of a low frequency millennial oscillation in western Mediterranean climate: implications for past dynamics of the North Atlantic atmospheric westerlies. The Holocene 23, 153–166.

Frigola, J., Moreno, A., Cacho, I., Canals, M., Sierro, F.J., Flores, J.A., Grimalt, J.O., Hodell, D.A., Curtis, J.H., 2007. Holocene climate variability in the western Mediterranean region from a deepwater sediment record. Paleoceanography 22, 2209.

Geraga, M., Mylona, G., Tsaila-Monopoli, S., Papatheodorou, G., Ferentinos, G., 2008. Northeastern Ionian Sea: palaeoceanographic variability over the last 22 ka. J. Mar. Syst. 74, 623–638.

Gogou, A., Triantaphyllou, M.V., Parinos, C.S., Athanasiou, M., Bouloubassi, I., Roussakis, G., Dimiza, M.D., Kamberi, E., Thanasoura, E., Giannouli, M., Lykousis, V., 2012. Temperature reconstructions and paleoceanographic changes during the last 2 millenia in the north Aegean Sea (northeastern Mediterranean). MedCLIVAR Conference, book of abstracts 43.

Gogou, A., Triantaphyllou, M., Xoplaki, E., Izdebski, A., Parinos, C., Dimiza, M., Bouloubassi, I., Luterbacher, J., Kouli, K., Martrat, B., Toreti, A., Fleitmann, D., Rousakis, G., Kaberi, H., Athanasiou, M., Lykousis, V., 2016. Climate variability and socio-environmental changes in the northern Aegean (NE Mediterranean) during the last 1500 years. Quat. Sci. Rev. http://dx.doi.org/10.1016/j.quascirev.2016.01.009.

Goudeau, M.L.S., Reichart, G.J., Wit, J.C., deNooijer, L.J., Grauel, A.L., Bernasconi, S.M., de Lange, G.J., 2015. Seasonality variations in the Central Mediterranean during climate change events in the Late Holocene. Palaeogeogr. Palaeoclimatol. Palaeoecol. 418, 304–318.

Goy, J.L., Zazo, C., Dabrio, C.J., 2003. A beach-ridge progradation complex reflecting periodical sea-level and climate variability during the Holocene (Gulf of Almeria, Western Mediterranean). Geomorphology 50, 251–268.

Grauel, A.L., Goudeau, M.L.S., de Lange, G.J., Bernasconi, S.M., 2013. Climate of the past 2500 years in the Gulf of Taranto, central Mediterranean Sea: a high-resolution climate reconstruction based on δ^{18}O and δ^{13}C of *Globigerinoides ruber* (white). The Holocene 23, 1440–1446.

Greatbatch, R.J., 2000. The North Atlantic Oscillation. Stochastic Environmental Research and Risk Assessment Vol. 14,. Springer-Verlag, p. 213.

Häkkinen, S., Rhines, P.B., Worthen, D.L., 2011. Atmospheric blocking and Atlantic Multidecadal Ocean variability. Science 334, 655–659.

Hemleben, C., Spindler, M., Anderson, O.R., 1989. Modern Planktonic Foraminifera. Springer-Verlag, New York, p. 363.

Holmgren, K., Gogou, A., Izdebski, A., Luterbacher, J., Sicre, M.A., Xoplaki, E., 2015. Mediterranean Holocene climate, environment and human societies. Quat. Sci. Rev. http://dx.doi.org/10.1016/j.quascirev.2015.12.014.

Iermano, I., Liguori, G., Iudicone, D., Buongiorno Nardelli, B., Colella, S., Zingone, A., Saggiomo, V., Ribera d'Alcalà, M., 2012. Filament formation and evolution in buoyant coastal waters: observation and modelling. Prog. Oceanogr. 106, 118–137.

Incarbona, A., Ziveri, P., Di Stefano, E., Lirer, F., Mortyn, G., Patti, B., Pelosi, N., Sprovieri, M., Tranchida, G., Vallefuoco, M., Albertazzi, S., Bellucci, L.G., Bonanno, A., Bonomo, S., Censi, P., Ferraro, L., Giuliani, S., Mazzola, S., Sprovieri, R., 2010. The impact of the Little Ice Age on Coccolithophores in the central Mediterranean Sea. Clim. Past 6, 795–805.

Jalali, B., Sicre, M.A., Bassetti, M.A., Kallel, N., 2015. Holocene climate variability in the North-western Mediterranean Sea (Gulf of Lions). Clim. Past Discuss. 11, 3187–3209.

Jalut, G., Esteban Amat, A., Mora, S.R., Fontugne, M., Mook, R., Bonnet, L., Gauquelin, T., 1997. Holocene climatic changes in the western Mediterranean: installation of the Mediterranean climate. C. R. Acad. Sci. III 325, 327–334.

Jalut, G., Esteban Amat, A., Bonne, L., Gauquelin, T., Fontugne, M., 2000. Holocene climatic changes in the western Mediterranean, from south-East France to south-East Spain. Palaeogeogr. Palaeoclimatol. Palaeoecol. 160, 255–290.

Jalut, G., Dedoubat, J.J., Fontugne, M., Otto, T., 2009. Holocene circum-Mediterranean vegetation changes: climate forcing and human impact. Quat. Int. 200, 4–18.

Joannin, S., Brugiapaglia, E., de Beaulieu, J.-L., Bernardo, L., Magny, M., Peyron, O., Goring, S., Vannière, B., 2012. Pollen-based reconstruction of Holocene vegetation and climate in southern Italy: the case of Lago Trifoglietti. Clim. Past 8, 1973–1996.

Jones, P., Mann, D., Mann, M.E., 2004. Climate over past millennia. Rev. Geophys. 42, RG2002.

Jonkers, L., Brummer, G.J.A., Peeters, F.J.C., van Aken, H.M., De Jong, M.F., 2010. Seasonal stratification, shell flux, and oxygen isotope dynamics of left-coiling *N. pachyderma* and *T. quinqueloba* in the western subpolar North Atlantic. Paleoceanography 25, PA2204.

Jorissen, F.J., Barmawidjaja, D.M., Puskaric, S., van der Zwaan, G.J., 1992. Vertical distribution of benthonic foraminifera in the northern Adriatic Sea: the relation with the organic flux. Mar. Micropaleontol. 19, 131–146.

Kirschvink, J.L., 1980. The least-squares line and plane and the analysis of palaeomagnetic data. Geophys. J. R. Astron. Soc. 62, 699–718.

Krivosheya, V.G., Ovchinnikov, I.M., 1973. Properties of the geostrophic circulation of the Tyrrhenian Sea. Oceanology 13, 996–1002.

Kucera, M., Weinelt, M., Kiefer, T., Pflaumannb, U., Hayesa, A., Weinelte, M., Chenf, M.T., Mixg, A.C., Barrowsh, T.T., Cortijoi, E., Dupratj, J., Jugginsk, S., Waelbroecki, C., 2005. Reconstruction of sea-surface temperatures from assemblages of planktonic foraminifera: multi-technique approach based on geographically constrained calibration data sets and its application to glacial Atlantic and Pacific Oceans. Quat. Sci. Rev. 24, 951–998.

Lamb, H.H., 1977. Climate: Present, Past and Future vol. 2. Methuen & Co, London.

Le, J., Shackleton, N.J., 1994. Reconstructing paleoenvironment by transfer function: model evaluation with simulated data. Mar. Micropaleontol. 24, 187–199.

Le Maitre, R.W., 2005. Igneous Rocks. A Classification and Glossary of Terms. Recommendations of the International Union of Geological Sciences Subcommission on the Systematics of Igneous Rocks. Cambridge University Press, Cambridge, p. 256.

Lionello, P., 2012. The Climate of the Mediterranean Region: From the Past to the Future. E. Science, Burlington, MA.

Lirer, F., Sprovieri, M., Ferraro, L., Vallefuoco, M., Capotondi, L., Cascella, A., Petrosino, P., Insinga, D.D., Pelosi, N., Tamburrino, S., Lubritto, C., 2013. Integrated stratigraphy for the late Quaternary in the eastern Tyrrhenian Sea. Quat. Int. 292, 71–85.

Lirer, F., Sprovieri, M., Vallefuoco, M., Ferraro, L., Pelosi, N., Giordano, L., Capotondi, L., 2014. Planktonic foraminifera as bio-indicators for monitoring the climatic changes that have occurred over the past 2000 years in the southeastern Tyrrhenian Sea. Integr. Zool. 9, 542–554.

Lisiecki, L.E., Lisiecki, P.A., 2002. Application of dynamic programming to the correlation of paleoclimate records. Paleoceanography 17, 1049.

López-Moreno, J.I., Vicente-Serrano, S.M., Morán-Tejeda, E., Lorenzo-Lacruz, J., Kenawy, A., Beniston, M., 2011. Effects of the North Atlantic Oscillation (NAO) on combined temperature and precipitation winter modes in the Mediterranean mountains: observed relationships and projections for the 21st century. Glob. Planet. Chang. 77, 62–76.

Lurcock, P.C., Wilson, G.S., 2012. PuffinPlot: a versatile, user-friendly program for paleomagnetic analysis. Geochem. Geophys. Geosyst. 13, Q06Z45.

Luterbacher, J., García-Herrera, R., Akcer-On, S., Allan, R., Alvarez-Castro, M.C., Benito, G., Booth, J., Büntgen, U., Cagatay, N., Colombaroli, D., Davis, B., Esper, J., Felis, T., Fleitmann, D., Frank, D., Gallego, D., Garcia-Bustamante, E., Glaser, R., Gonzàlez-Rouco, J.F., Goosse, H., Kiefer, T., Macklin, M.G., Manning, S., Montagna, P., Newman, L., Power, M.J., Rath, V., Ribera, P., Riemann, D., Roberts, N., Sicre, M., Silenzi, S., Tinner, W., Valero-Garces, B., van der Schrier, G., Tzedakis, C., Vannière, B., Vogt, S., Wanner, H., Werner, J.P., Willett, G., Williams, M.H., Xoplaki, E., Zerefos, C.S., Zorita, E., 2012. A review of 2000 years of paleoclimatic evidence in the Mediterranean. In: Lionello, P. (Ed.), The Climate of the Mediterranean Region: From the Past to the Future. Elsevier, Amsterdam, The Netherlands, pp. 87–185.

Mackensen, A., Douglas, R.G., 1989. Down-core distribution of live and dead deep-water benthonic foraminifera in box cores from the Weddell Sea and the California Borderland. Deep-Sea Res. 36, 879–900.

Macklin, M.G., Benito, G., Gregory, K.J., Johnstone, E., Lewin, J., Michczynska, D.J., Soja, R., Starkel, L., Thorndycraft, V.R., 2006. Past hydrological events reflected in the Holocene fluvial record of Europe. Catena 66, 145–154.

Magny, M., Miramont, C., Sivan, O., 2002. Assessment of the impact of climate and anthropogenic factors on Holocene Mediterranean vegetation in Europe on the basis of palaeohydrological records. Palaeogeogr. Palaeoclimatol. Palaeoecol. 186, 47–59.

Magny, M., Combourieu Nebout, N., de Beaulieu, J.L., Bout-Roumazeilles, V., Colombaroli, D., Desprat, S., Francke, A., Joannin, S., Peyron, O., Revel, M., Sadori, L., Siani, G., Sicre, M.A., Samartin, S., Simonneau, A., Tinner, W., Vannière, B., Wagner, B., Zanchetta, G., Anselmetti, F., Brugiapaglia, E., Chapron, E., Debret, M., Desmet, M., Didier, J., Essallami, L., Galop, D., Gilli, A., Haas, J.N., Kallel, N., Millet, L., Stock, A., Turon, J.L., Wirth, S., 2013. North-south palaeohydrological contrasts in the central Mediterranean during the Holocene: tentative synthesis and working hypotheses. Clim. Past 9, 2043–2071.

Malanotte-Rizzoli, P., Artale, V., Borzelli-Eusebi, G.L., Brenner, S., Civitarese, G., Crise, A., 2014. Physical forcing and physical/biochemical variability of the Mediterranean Sea: a review of unresolved issues and directions for future research. Ocean Sci. 10, 281–322.

Mann, M.E., Zhang, Z., Rutherford, S., Bradley, R.S., Hughes, M.K., Shindell, D., Ammann, C., Faluvegi, G., Ni, F., 2009. Global signatures and dynamical origins of the Little Ice Age and Medieval Climate Anomaly. Science 326, 1256–1260.

Martínez Cortizas, A., Potevedra-Pombal, X., García-Rodeja, E., Nóvoa-Muñoz, J.C., Shotyk, W., 1999. Mercury in a Spanish peat bog: archive of climate change and atmospheric metal deposition. Science 284, 939–942.

Martìn-Puertas, C., Matthes, K., Brauer, A., Muscheler, R., Hansen, F., Petrick, C., Aldahan, A., Possnert, G., van Geel, B., 2012. Regional atmospheric circulation shifts induced by a grand solar minimum. Nat. Geosci. 5, 397–401.

Maselli, V., Trincardi, F., 2013. Man made deltas. Nat. Sci. Rep. 3 (1926), 1–7.

Mastrolorenzo, G., Munno, R., Rolandi, G., 1993. Vesuvius 1906: a case study of a paroxysmal eruption and its relation to eruption cycles. J. Volcanol. Geotherm. Res. 58, 217–237.

Mayewski, P.A., Rohling, E., Stager, C., Karlén, W., Maasch, K.A., Meeker, L.D., Meyerson, E.A., Gasse, F., van Kreveld, S., Holmgren, K., Lee-Thorp, J., Rosqvist, G., Rack, F., Staubwasser, M., Schneider, R.R., Steig, E.J., 2004. Holocene climate variability. Quat. Res. 62, 243–255.

Millot, C., 1987. Circulation in the western Mediterranean Sea. Oceanol. Acta 10, 143–149.

Moffa Sánchez, P., Born, A., Hall, I.R., Thornalley, D.J.T., Barker, S., 2014. Solar forcing of North Atlantic surface temperature and salinity over the past millennium. Nat. Geosci. 7 (4), 275–278.

Moreno, A., Pérez, A., Frigola, J., Nieto-Moreno, V., Rodrigo-Gámiz, M., Martrat, B., González-Sampériz, P., Morellón, M., Martín-Puertas, C., Corella, J.P., Belmonte, A., Sancho, C., Cacho, I., Herrera, G., Canals, M., Grimalt, J.O., Jiménez-Espejo, F., Martínez-Ruiz, F., Vegas-Vilarrúbia, T., Valero-Garcés, B.L., 2012. The Medieval Climate Anomaly in the Iberian Peninsula reconstructed from marine and lake records. Quat. Sci. Rev. 43, 16–32.

Nieto-Moreno, V., 2012. Late Holocene Climatic Variability in the Western Mediterranean: An Integrated Organic and Inorganic Multyproxy Approach (Ph.D. Thesis) Istituto Andaluz de Ciencias de la Tierra (CSIC-UGR), Universidad de Granada (UGR), Granada, Spain.

Nieto-Moreno, V., Martìnez-Ruiz, F., Giralt, S., Jiménez-Espejo, F., Gallego-Torres, D., Rodrigo-Gàmiz, M., Garcìa-Orellana, J., Ortega-Huertas, M., de Lange, G.J., 2011. Tracking climate variability in the western Mediterranean during the Late Holocene: a multiproxy approach. Clim. Past 7, 1395–1414.

Nieto-Moreno, V., Martínez-Ruiz, F., Willmott, V., García-Orellana, J., Masqué, P., Sinninghe Damsté, J.S., 2013. Climate conditions in the westernmost Mediterranean over the last two millennia: an integrated biomarker approach. Org. Geochem. 55, 1–10.

Numberger, L., Hemleben, C., Hoffmann, R., Mackensen, A., Schulz, H., Wunderlich, J.M., Kucera, M., 2009. Habitats, abundance patterns and isotopic signals of morphotypes of the planktonic foraminifer *Globigerinoides ruber* (d'Orbigny) in the eastern Mediterranean Sea since the Marine Isotopic Stage 12. Mar. Micropaleontol. 73 (1–2), 90–104. http://dx.doi.org/10.1016/j.marmicro.2009.07.004.

Oldfield, T.E.E., Smith, R.J., Harrop, S.R., Leader-Williams, N., 2003. Field sports and conservation in the United Kingdom. Nature 423, 531–533.

Olsen, J., Anderson, N.J., Knudsen, M.F., 2012. Variability of the North Atlantic Oscillation over the past 5200 years. Nat. Geosci. 5, 808–812.

Pavón-Carrasco, F.J., Osete, M.L., Torta, J.M., Santis, A.D., 2014. A geomagnetic field model for the Holocene based on archaeomagnetic and lava flow data. Earth Planet. Sci. Lett. 388, 98–109.

Pierini, S., Simioli, A., 1998. A wind-driven circulation model of the Tyrrhenian Sea area. Journal of Marine Systems 18, 161–178.

Piva, A., Asioli, A., Trincardi, F., Schneider, R.R., Vigliotti, L., 2008a. Late Holocene climate variability in the Adriatic Sea (Central Mediterranean). The Holocene 18, 153–167.

Piva, A., Asioli, A., Schneider, R.R., Trincardi, F., Andersen, N., Colmenero-Hidalgo, E., Dennielou, B., Flores, J.A., Vigliotti, L., 2008b. Climatic cycles as expressed in sediments of the PROMESS1 borehole PRAD1-2, central Adriatic, for the last 370 ka: integrated stratigraphy. Geochem. Geophys. Geosyst. 9.

Pujol, C., Vergnaud Grazzini, C., 1995. Distribution patterns of live planktic foraminifers as related to regional hydrography and productive systems of the Mediterranean Sea. Mar. Micropaleontol. 25, 187–217.

Rathburn, A.E., Corliss, B.H., 1994. The ecology of living (stained) deep-sea benthonic foraminifera from the Sulu Sea. Paleoceanography 9, 87–150.

Ravelo, A.C., Fairbanks, R.G., Philander, S., 1990. Reconstructing tropical Atlantic hydrography using planktonic foraminifera and an ocean model. Paleoceanography 5, 409–431.

Reille, M., 1992. Pollen et spores d'Europe et d'Afrique du Nord. Laboratoire de botanique historique et palynologie. URA CNRS, Marseille, France, p. 520.

Reille, M., 1995. Pollen et spores d'Europe et d'Afrique du Nord. Supplement 1. Laboratoire de botanique historique et palynologie. URA CNRS, Marseille, France, p. 327.

Reille, M., 1998. Pollen et spores d'Europe et d'Afrique du Nord. Supplement 2. Laboratoire de botanique historique et palynologie. URA CNRS, Marseille, France, p. 521.

Roberts, N., Brayshaw, D., Kuzucuoglu, C., Perez, R., Sadori, L., 2011. The Mid-Holocene climatic transition in the Mediterranean: causes and consequences. The Holocene 21, 3–13.

Roberts, N., Moreno, A., Valero-Garcés, B.L., Corella, J.P., Jones, M., Allcock, S., Woodbridge, J., Morellón, M., Luterbacher, J., Xoplaki, E., Türkeş, M., 2012. Palaeolimnological evidence for an east–west climate see-saw in the Mediterranean since AD 900. Glob. Planet. Chang. 84-85, 23–34.

Robinson, A.R., Golnaraghi, M., 1994. The Physical and Dynamical Oceanography of the Mediterranean. In: Malanotte-Rizzoli, P., Robinson, A.R. (Eds.), Ocean Processes in Climate Dynamics: Global and Mediterranean Examples. The Netherlands. Kluwer Academic Publishers, Dordrecht, pp. 255–306.
Rohling, E.J., Mayewski, P.A., Abu-Zied, R.H., Casford, J.S.L., Hayes, A., 2002. Holocene atmosphere–ocean interactions: records from Greenland and the Aegean Sea. Clim. Dyn. 18, 587–593.
Rouis-Zargouni, I., Turon, J.L., Londeix, L., Essallami, L., Kallel, N., Sicre, M.A., 2010. Environmental and climatic changes in the central Mediterranean Sea (Siculo–Tunisian Strait) during the last 30 ka based on dinoflagellate cyst and planktonic foraminifera assemblages. Palaeogeogr. Palaeoclimatol. Palaeoecol. 285, 17–29.
Sacchi, E., Conti, M.A., D'Orazi Porchetti, S., Logoluso, A., Nicosia, U., Perugini, G., Petti, F.M., 2009. Aptian dinosaur footprints from the Apulia platform (Bisceglie, southern Italy) in the framework of the periadriatic ichnosites. Palaeogeogr. Palaeoclimatol. Palaeoecol. 271, 104–116.
Sacchi, M., Pepe, F., Corradino, M., Insinga, D.D., Molisso, F., 2014. The Neapolitan Yellow Tuff caldera offshore the Campi Flegrei: stratal architecture and kinematic reconstruction during the last 15 ky. Mar. Geol. 354, 15–33.
Sadori, L., Narcisi, B., 2001. The postglacial record of environmental history from Lago di Pergusa (Sicily). The Holocene 11, 655–671.
Sadori, L., Giraudi, C., Masi, A., Magny, M., Ortu, E., Zanchetta, G., Izdebski, A., 2015. Climate, environment and society in southern Italy during the last 2000 years. A review of the environmental, historical and archaeological evidence. Quat. Sci. Rev. http://dx.doi.org/10.1016/j.quascirev.2015.09.0.
Sanchez-Cabeza, J.A., Ruiz-Fernández, A.C., 2012. ^{210}Pb sediment radiochronology: an integrated formulation and classification of dating models. Geochim. Cosmochim. Acta 82, 183–200.
Sangiorgi, F., Capotondi, L., Combourieu Nebout, N., Vigliotti, L., Brinkhuis, H., Giunta, S., Lotter, A.F., Morigi, C., Negri, A., Reichart, G.J., 2003. Holocene seasonal sea-surface temperature variations in the southern Adriatic Sea inferred from a multiproxy approach. J. Quat. Sci. 18, 723–732.
Santacroce, R., Cioni, R., Marianelli, P., Sbrana, A., Sulpizio, R., Zanchetta, G., Donahue, D.J., Joron, J.L., 2008. Age and whole rock-glass compositions of proximal pyroclastics from the major explosive eruptions of Somma–Vesuvius: a review as a tool for distal tephrostratigraphy. J. Volcanol. Geotherm. Res. 177, 1–18.
Schilman, B., Bar-Matthews, M., Almogi-Labin, A., Luz, B., 2011. Global climate instability reflected by Eastern Mediterranean marine records during the late Holocene. Palaeogeogr. Palaeoclimatol. Palaeoecol. 176, 157–176.
Sen Gupta, B.K., Machain-Castillo, M.L., 1993. Benthonic foraminifera in oxygen poor habitats. Mar. Micropaleontol. 20, 183–201.
Siani, G., Magny, M., Paterne, M., Debret, M., Fontugne, M., 2013. Paleohydrology reconstruction and Holocene climate variability in the South Adriatic Sea. Clim. Past 9, 499–515.
Sicre, M.A., Jacoba, J., Ezata, U., Roussea, S., Kissela, C., Yioua, P., Eiríksson, J., Knudsenc, K.L., Jansend, E., Turone, J.L., 2008. Decadal variability of sea surface temperatures off North Iceland over the last 2000 yrs. Earth Planet. Sci. Lett. 268, 137–142.
Smith, V.C., Isaia, R., Pearce, N.J.G., 2011. Tephrostratigraphy and glass compositions of post-15 kyr Campi Flegrei eruptions: implications for eruption history and chronostratigraphic markers. Quat. Sci. Rev. 30, 3638–3660.
Spooner, M.I., Barrows, T.T., De Deckker, P., Paterne, M., 2005. Palaeoceanography of the Banda Sea, and Late Pleistocene initiation of the Northwest Monsoon. Glob. Planet. Chang. 49, 28–46.
Spötl, C., Vennemann, T.W., 2003. Continuous-flow isotope ratio mass spectrometric analysis of carbonate minerals. Rapid Commun. Mass Spectrom. 17, 1004–1006.
Sprovieri, R., Di Stefano, E., Incarbona, A., Gargano, M.E., 2003. A high-resolution of the last deglaciation in the Sicily Channel based on foraminiferal and calcareous nannofossil quantitative distribution. Palaeogeogr. Palaeoclimatol. Palaeoecol. 202, 119–142.
Staubwasser, M., Weiss, H., 2006. Holocene climate and cultural evolution in Late Prehistoric–Early Historic West Asia. Quat. Res. 66, 371–504.
Stockmarr, J., 1971. Tablets with spores used in absolute pollen analysis. Pollen Spores 13, 615–621.
Taricco, C., Ghil, M., Alessio, S., Vivaldo, G., 2009. Two millennia of climate variability in the Central Mediterranean. Clim. Past 5, 171–181.
Taricco, C., Vivaldo, G., Alessio, S., Rubinetti, S., Mancuso, S., 2015. A high-resolution δ^{18}O record and Mediterranean climate variability. Clim. Past 11, 509–522.
Tinner, W., van Leeuwen, J.F.N., Colombaroli, D., Vescovi, E., van der Knaap, W.O., Henne, P.D., Pasta, S., La Mantia, T., 2009. Holocene environmental and climatic changes at Gorgo Basso, a coastal lake in southern Sicily, Italy. Quat. Sci. Rev. 28, 1498–1510.
Tomozeiu, R., Lazzeri, M., Cacciamani, C., 2002. Precipitation fluctuations during winter season from 1960 to 1995 over Emilia—Romagna, Italy. Theor. Appl. Climatol. 72, 221–229.
Trouet, V., Esper, J., Graham, N.E., Baker, A., Scourse, J.D., Frank, D.C., 2009. Persistent positive North Atlantic Oscillation mode dominated the medieval climate anomaly. Science 324, 78–80.
Vallefuoco, M., Lirer, F., Ferraro, L., Pelosi, N., Capotondi, L., Sprovieri, M., Incarbona, A., 2012. Climatic variability and anthropogenic signatures in the Gulf of Salerno (southerneastern Tyrrhenian Sea) during the last half millennium. Rend. Fisici Accad. Lincei 23, 13–23.
Van Geel, B., Heusser, C.J., Renssen, H., Schuurmans, C.J.E., 2000. Climatic change in Chile at around 2700 BP and global evidence for solar forcing: a hypothesis. The Holocene 10, 659–664.
Vezzoli, L., Principe, C., Malfatti, J., Arrighi, S., Tanguy, J.C., Le Goff, M., 2009. Modes and times of caldera resurgence: the <10 ka evolution of Ischia Caldera, Italy, from high-precision archaeomagnetic dating. J. Volcanol. Geotherm. Res. 186, 305–319.
Walker, M.J.C., Berkelhammer, M., Bjorck, S., Cwynar, L.C., Fisher, D.A., Long, A.J., Lower, J.J., Newnham, R.M., Rasmussen, S.O., Weiss, H., 2012. Formal subdivision of the Holocene series/epoch: a discussion paper by a working group of INTIMATE (integration of ice-core, marine and terrestrial records) and the subcommission on quaternary stratigraphy (International Commission on Stratigraphy). J. Quat. Sci. 27, 649–659.
Wang, L.J., 2000. Isotopic signals in two morphotypes of *Globigerinoides ruber* (white) from the South China Sea: implications for monsoon climate change during the last glacial cycle. Palaeogeogr. Palaeoclimatol. Palaeoecol. 161 (3–4), 381–394.
Wanner, H., Brönnimann, S., Casty, C., Gyalistras, D., Luterbacher, J., Schmutz, C., Stephenson, D.B., Xoplaki, E., 2001. North Atlantic Oscillation — concepts and studies. Surv. Geophys. 22, 321–382.
Xoplaki, E., Jones, P., Herrera, R.G., Besonen, M., Diaz, H., Gershunov, A., Zerefos, C., Giannakopoulos, C., Griggs, C., Raible, C., Tourre, Y.M., 2008. Symposium report: "climate extremes during recent millennia and their impact on mediterranean societies". Workshop Reports.
Zanchetta, G., Sulpizio, R., Roberts, N., Cioni, R., Eastwood, W.J., Siani, G., Caron, B., Paterne, M., Santacroce, R., 2011. Tephrostratigraphy, chronology and climatic events of the Mediterranean basin during the Holocene: an overview. The Holocene 21 (1), 33–52.
Zolitschka, B., Behre, K.E., Schneider, J., 2003. Human and climatic impact on the environment as derived from colluvial, fluvial and lacustrine archives—examples from the Bronze Age to the Migration period, Germany. Quat. Sci. Rev. 22, 81–100.